Available online at www.sciencedirect.com
SCIENCE DIRECT®
Journal of Sound and Vibration 296 (2006) 651–675
JOURNAL OF SOUND AND VIBRATION
www.elsevier.com/locate/jsvi

Vibrations and stability of a flexible disk rotating in a gas-filled enclosure—Part 1: Theoretical study

Namcheol Kang, Arvind Raman*

Mechanical Engineering, Purdue University, 585 Purdue Mall, West Lafayette, IN 47907-2088, USA

Received 14 December 2004; received in revised form 4 August 2005; accepted 10 September 2005
Available online 13 December 2005

Abstract

The vibrations and linear stability of a flexible disk rotating at sub- and supercritical speeds, and coupled to the acoustic oscillations of the surrounding fluid are investigated theoretically. The surrounding fluid is contained in a cylindrical enclosure. The coupled gyroscopic system equations are formulated using a Kirchhoff plate model for the disk, and the wave equation for the compressible fluid. The formulation includes systematically the effects of geometric perturbations such as radial clearances and asymmetric disk positioning, as well as bulk rotating fluid flows driven by fluid viscosity and disk rotation. A rigorous spatial discretization of this coupled gyroscopic system leads to a singular generalized non-Hermitian eigenvalue problem for which a special computational treatment is presented. The underlying physics of acoustic–structure coupling in the presence of these effects is complex—acoustic oscillations of the fluid above and below the disk couple through disk vibrations and through the radial clearance, while the bulk fluid rotation splits the acoustic modes into forward and backward traveling waves. Flutter instabilities arising from acoustic–structure mode coalescence and various damping mechanisms are discussed. The predictions reveal significant influences of radial clearance, asymmetric disk positioning, and bulk fluid rotation on the vibration and acoustic characteristics of the system that are likely to be observed in experiments, and in practical applications such as in CD/DVD drives and hard disk drives.

1. Introduction

The dynamics and vibrations of thin rotating disks pose significant engineering challenges in a wide variety of industrial applications—in data storage systems including CD/DVD ROMs, hard disk drives [1,2]; in manufacturing applications including circular saws; in turbomachinery including conventional and micro-fabricated gas turbines [3]; and in chemical applications including biochemical filtration technologies [4]. In applications where the disk rotates in an enclosure filled with a gas, acoustic–structure interactions can adversely affect the stability, and noise, vibration and harshness characteristics of the device.

Broadly speaking, literature on the vibration and stability of rotating disks coupled to surrounding fluids can be divided into three categories. In the first category, hydrodynamic lubrication theories are typically used to model a thin gas film adjacent to the rotating flexible disk [5–8]. These models are generally valid at low gas

*Corresponding author. Tel.: +1 765 494 5733; fax: +1 765 494 0539.
E-mail address: raman@ecn.purdue.edu (A. Raman).

0022-460X/$ - see front matter © 2005 Elsevier Ltd. All rights reserved.
doi:10.1016/j.jsv.2005.09.001

Nomenclature

A_R, A_d, A_u rigid, disk, and unbaffled surface area, respectively
a_n, b_n generalized coordinates of upper and lower enclosures, respectively
b_c^*, b_u^* constrained and unconstrained generalized coordinates, respectively
C ratio of acoustic speed to a bending wave speed of the stationary disk ($= c_o/R_oT_o$)
c_o acoustic speed of the surrounding fluid
D disk flexural rigidity ($= EH^3/12(1-v^2)$)
E Young's modulus of the disk material
F_n acoustic normal modes of the enclosure
H thickness of the disk
$\mathbf{K}_d[\,\cdot\,]$ self-adjoint and positive definite stiffness operator of the rotating disk
L, l air gap between the disk and top/bottom cover of the enclosure
L_{nm}, $\boldsymbol{L}_{nm}$ acoustic–structure coupling coefficient and its submatrix, respectively
(m_1, m_2) nodal diameter and nodal circle modes of the disk
N number of basis function of disk and acoustic modes in one dimension
$\boldsymbol{N}_{\text{membrane}}$ number of basis function of membrane used for unbaffled region
N_{nr}, $\boldsymbol{N}_{nr}$ inter-cavity coupling coefficient and its submatrix, respectively
(n_1, n_2, n_3) nodal diameter, nodal circle, and z-directional node number of the enclosure
Q resultant pressure on the disk
q_m, u_r generalized coordinates of disk and membrane for unbaffled region, respectively
R_i, R_o inner and outer radii of the disk, respectively
(r_1, r_2) nodal diameter and nodal circle modes of the membrane
$\mathbf{T}$ transformation matrix to reduce constraint equations
T_o nondimensional time constant
$\mathbf{u}'$ the velocity perturbation of the flow
V volume of the enclosure
W, w transverse displacements of disk

Greek letters

Γ acoustic energy to total energy ratio in the mode
ζ transverse displacements of membrane
κ clamping ratio of the disk ($= R_i/R_o$)
Λ ratio of the fluid to disk mass density ($= \rho_f R_o/\rho_d H$)
Λ_n nth uncoupled acoustical natural frequency
v Poisson's ratio of the disk material
ρ_d mass density of the disk
ρ_f mass density of the fluid
σ_R, σ_θ radial and circumferential stresses, respectively
Φ, ϕ velocity potential of the acoustic enclosure
ψ_m, φ_r in vacuo disk and membrane modes, respectively
Ω nondimensionalized rotating speed of the disk
Ω_d dimensionalized rotating speed of the disk
Ω_f nondimensionalized rotating speed of the surrounding fluid
ω eigenvalues, where $\lambda = \omega^2$

Superscripts

$(\,)^*$ dimensional variables
a, b upper and lower enclosures, respectively
C, S cosine and sine components, respectively
$(\cdot)$ temporal derivatives
in, out in-phase and out-of-phase acoustic modes, respectively
$\sim$, $\wedge$ common and distinct parts of matrices, respectively
T transpose of a matrix

Subscripts

$(\,)_{,(\,)}$ spatial derivatives
F, B, R quantities related to forward, backward, reflective traveling waves, respectively

Acronyms

FTW forward traveling wave
BTW backward traveling wave
RTW reflective traveling wave
Re, Im real and imaginary part of eigenvalues, respectively

Reynolds numbers such as those found in floppy or zip disk applications. In the second category, several researchers have either used ad hoc rotating damping models to predict flutter in enclosed and unenclosed disks [9–12], or discrete springs to model acoustic coupling between disks in disk stacks [13,14]. While they may be appropriate for explaining instabilities and certain vibration coupling phenomena in these systems, these models are not entirely predictive in the sense that several model coefficients need to be determined experimentally. The last category concerns the use of bona fide continuum models for both the fluid and the rotating disk such as the works by Renshaw et al. [15], and the authors [16]. Such models are particularly relevant for industrial applications such as CD/DVD ROMs and hard disk drives where Reynolds numbers are high rendering inapplicable lubrication-type fluid models. Furthermore, in these applications the frequencies of acoustic oscillations of the enclosure are typically of the same order of magnitude as some disk vibration frequencies. Renshaw et al. [15] first investigated the aeroelastic stability of a flexible disk rotating in an enclosed compressible potential flow both theoretically and experimentally. Although the theoretically predicted trends agreed qualitatively with experimental observations, the instability mechanisms and the acoustic–structure interactions were not discussed.

For these reasons, the authors recently investigated the acoustic–structure interactions and instability mechanisms of a flexible rotating disk rotating in an enclosed compressible potential fluid [16]. However, this previous study investigated a simple geometry for the problem neglecting radial gap and assuming a symmetric placement of the disk in the enclosure. Further, this work neglected the effects of bulk rotations of the surrounding fluid that are naturally induced by disk rotation in the enclosure. In industrial applications such as in hard disk or CD/DVD drives, disks rotate with a radial clearance between disk and sidewall of the enclosure, and are often not symmetrically placed in the enclosure. In addition, as the disk rotates, the surrounding fluid is not stationary any more but is driven into complex rotational motions. As will be justified later in the paper, this fluid flow can be approximated as a rigidly rotating bulk flow for the purposes of studying acoustic interactions.

Not only do these geometric perturbations and rotating bulk fluid flows affect significantly the system dynamics and stability, their inclusion leads to specific mathematical challenges that are not present in the simplified problem studied earlier by the authors [16]. For instance, the presence of a radial clearance leads to mixed boundary conditions in the coupled partial differential equations governing acoustic and disk oscillations, and this eventually leads to singular terms in the discretized form of the coupled eigenvalue problem. Likewise, the presence of rotating bulk fluid flow generates additional, previously unaccounted for, Coriolis and centripetal accelerations terms in the governing equations for the surrounding compressible fluid. For these reasons, an investigation of these practically important geometric perturbations and rotating bulk fluid flows simply cannot be undertaken within the prior mathematical formulation by the authors.

This study examines the effect of two geometric perturbations and rotating bulk fluid flows on the acoustic–structure interactions and instability mechanisms of a flexible rotating disk in an enclosed compressible fluid. The results are compared against prior research by the authors [16], which dealt with initially quiescent fluids and idealized enclosure geometry. Two key techniques to overcome the associated mathematical challenges are presented in Section 2 along with discretized system of equations. In Section 3, the discretized system in the presence of a radial clearance is investigated. Detailed convergence studies are performed to ensure the fidelity of the computational results, and the acoustic–structure interactions are studied. In Section 4, the effects of asymmetric disk positioning are investigated. The computational predictions in the presence of rotating bulk fluid flow and the effect of disk, acoustic and fluid damping are described in Sections 5 and 6, respectively. Finally the discussion and conclusions are presented in Section 7.

2. Coupled field equations and discretization

2.1. Derivation of coupled equations of motion in the absence of bulk rotating flow

Consider a uniform, thin annular disk, clamped at the inner and free at the outer radius, R_i and R_o, respectively, and rotating about its axis of symmetry at a constant angular speed Ω_d in a circular enclosure,

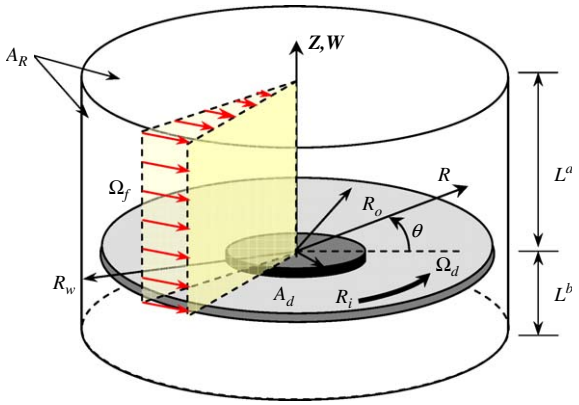

Fig. 1. A schematic diagram of the rotating disk in the presence of rotating bulk fluid flow in the cylindrical enclosure.

as shown in Fig. 1. The transverse vibrations of the rotating disk of thickness H and mass density ρ_d are modeled using the Kirchhoff plate theory for a homogeneous, isotropic, linearly elastic plate. Accordingly, E and v are the Young's modulus and Poisson's ratio of the disk material, respectively. The transverse deflections of the disk are described in an Eulerian representation using a ground-fixed cylindrical coordinate system (R, θ, Z). The undeflected disk mid-plane lies on $Z = 0$, and radial and circumferential stresses σ_R^* and σ_θ^* generated by disk rotation are derived from classical plane stress elasticity [17]. Based upon the above modeling assumptions, the field equation for the transverse vibrations of the rotating disk is subjected to external resultant pressure Q.

An initially quiescent, inviscid compressible potential surrounding fluid oscillates with small amplitude in the cylindrical enclosure. Assuming constant temperature, the fluid motion is governed by the standard wave equation of linear acoustics. Further, the Euler equation yields a linear relationship between the pressure field $P(R, \theta, Z; T)$ and fluid mass density ρ_f, at each point in the fluid domain. Therefore, the resultant pressure Q on the disk can be expressed as

$$Q = \rho_f(\Phi,_T^a - \Phi,_T^b)|_{Z=0} \equiv \rho_f[[\Phi,_T]]_{Z=0}, \tag{1}$$

where the superscripts a and b indicate the upper and lower enclosures relative to the disk mid-plane, respectively.

Following Ref. [16], dimensionless variables are introduced to obtain the dimensionless coupled partial differential equations governing disk and acoustic oscillations:

$$w,_{tt} + 2\Omega w,_{t\theta} + \Omega^2 w,_{\theta\theta} + \mathrm{K}_d[w] = \Lambda[[\phi,_t]]_{z=0}, \tag{2}$$

$$\nabla^2\phi = \frac{1}{C^2}\phi,_{tt}, \tag{3}$$

where

$$K_d[w] = \nabla^4 w - \frac{1}{r}(r\sigma_r w,_r),_r - \frac{1}{r^2}\sigma_\theta w,_{\theta\theta}. \tag{4}$$

$K_d[\,\cdot\,]$ is a self-adjoint and positive definite stiffness operator including bending and membrane stress effects. For reference, the dimensionless variables are defined in terms of the dimensional quantities as follows:

$$r = \frac{R}{R_o}, \quad \kappa = \frac{R_i}{R_o}, \quad z = \frac{Z}{R_o}, \quad w = \frac{W}{H}, \quad l^{a,b} = \frac{L^{a,b}}{R_o}, \quad t = \frac{T}{T_o}, \quad \Omega = \Omega_d T_o,$$
$$T_o = \sqrt{\frac{\rho_d R_o^4 H}{D}}, \quad \sigma_r = \frac{T_o^2}{\rho_d R_o^2}\sigma_r^*, \quad \sigma_\theta = \frac{T_o^2}{\rho_d R_o^2}\sigma_\theta^*, \quad \phi = \frac{T_o}{R_o H}\Phi, \tag{5}$$

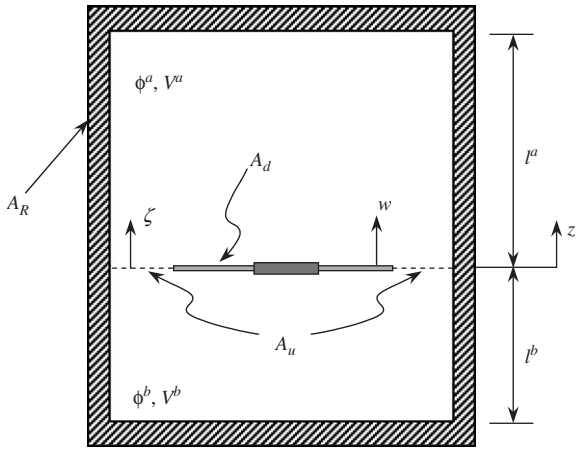

Fig. 2. Two-dimensional schematic diagram (in dimensionless variables) of the rotating disk and enclosure with a radial clearance.

and $\Lambda = \rho_f R_o/\rho_d H$ and $C = c_o/(R_o/T_o)$ are nondimensional parameters denoting, respectively, a scaled ratio of the fluid to disk mass density and the ratio of acoustic speed to a bending wave speed of the stationary disk.

The partial differential equations (2) and (3) are also subject to several boundary conditions. First, standard boundary conditions can be derived for the transverse vibration $w(r, \theta; t)$ assuming the rotating disk is clamped at the inner and free at the outer radius [15]. Secondly, three different surfaces bound the surrounding fluid—the flexible disk, rigid walls of the enclosure, and an artificial surface connecting the upper and lower enclosures. Normal fluid velocities satisfy the impermeability boundary conditions at the rigid walls over the area A_R, and the normal velocity matching condition on the disk surface over the area A_d. Finally, on the artificial surface in the radial clearance over the area A_u, the continuity of fluid velocity field (or equivalently the acoustic pressure) between upper and lower enclosures (see Fig. 2) needs to be enforced. These three boundary conditions are written as

$$\nabla\phi^{a,b} \cdot \mathbf{n} = \begin{cases} 0 & \text{on} \quad A_R, \\ \mp\dot{w} & \text{on} \quad A_d, \\ \mp\dot{\zeta} & \text{on} \quad A_u, \end{cases} \tag{6}$$

where $\mathbf{n}$ is the unit outward normal vector to the surface associated with the specific boundary condition. The $\mp$ sign indicates the opposing normal directions on the top and bottom side of the disk and the artificial surface over the radial clearance on A_u. Note that w and ϕ are unknown variables in the coupled equations, and $\dot{\zeta}$ is the unknown normal velocity field in the radial clearance A_u.

2.2. Problem formulation with rotating bulk fluid flow

While the earlier formulation assumes that the surrounding fluid is initially quiescent, in reality the disk rotation and fluid viscosity generate complex, unsteady flows in the enclosure. Incompressible, viscous fluid flows induced by rotating disks with and without enclosures have been the subject of a large body of literature in the fluid mechanics community starting early in the twentieth century by von Kármán [18] who studied the similarity solution for steady swirling flow over a rotating disk. Batchelor [19] investigated the flow between finitely spaced co-rotating disks and postulated that outside the thin viscous boundary layer on the disks, the fluid flow is essentially inviscid and consists of a rigidly rotating fluid core. Stewartson [20] also obtained similar solutions of a viscous fluid confined between two coaxial rotating disks both experimentally and theoretically. Following the studies of Batchelor and Stewartson, there has been a large body of literature concerning the flow between two rotating disks. For instance, Brady et al. [21] showed by means of asymptotic-numerical method that there exist multiple solutions between rotating disks depending on the end

conditions. Recently, flow visualization techniques using laser-Doppler velocimetry have confirmed the existence of the solid body rotation of the flow between co-rotating disks [22,23].

More relevant to the present scenario are works that focus on the fluid flow between one rotating disk and a cylindrical enclosure. Dijkstra et al. [24] used the finite difference method to compute the flow between two finite rotating disks enclosed by a cylinder, and compared the predictions with experimental results by means of stereophotography. According to their numerical and experimental results, viscous effects are mainly confined to the thin boundary layers on the disk and cylinder surfaces at low Ekman numbers, the ratio of viscous to Coriolis forces. Similarly, Escudier [25] showed the flow in a cylindrical container induced by a rotating endwall is determined by two parameters: the height-to-radius ratio and a rotation Reynolds number, and performed flow visualizations of the bulk rotating fluid flow in the enclosure at low Reynolds number. Recently, Soong et al. [26] performed a systematic study of the qualitative nature of three-dimensional flow structure between two rotating disks at a relatively wide range of rotational conditions, including the case where one disk is held fixed. They showed experimentally that the shroud near the disk rim is helpful to the formation of the large size rotating potential core in the enclosure.

Based on this literature, it can be deduced that purely rotating bulk fluid flow dominates global motion of the fluid between the rotating disk and stationary boundaries, provided aspect ratio and Reynolds number are suitable. The aspect ratio of the enclosure used in our study is comparable to those in the literature. Further, the disk rotation speed ranges studied in this paper (and in the accompanying experimental paper) cover all the Reynolds numbers studied in the above literature. Our interest in the present work is on understanding how these complex fluid flows affect acoustic–structure interactions. Accordingly, we focus on the acoustic oscillations superimposed on the potential core or rotating bulk fluid flow in the upper and lower enclosures. The same assumption was made in the work of Watanabe and Hara [27] for the theoretical instability analysis of a rotating disk in the presence of a rotating viscous incompressible fluid.

It is important to note that the unsteady or turbulent flows in the disk boundary layers or in the radial clearance are also of significant importance in data storage devices [28,29]. Several attempts have been made for the unsteady aerodynamic analysis of hard disk drives using the large eddy simulation model for turbulence [30,31]. However, it should also be noted that the structural motion due to the turbulence is assumed sufficiently small so that linear structural theory may be employed [32]. Accordingly, turbulent pressure fluctuations can be treated as forcing functions to disk and acoustic oscillations and are not discussed further.

Based on the above considerations, we assume an initial bulk fluid rotation in the enclosure at a prescribed rotation speed Ω_f, as shown in Fig. 1. The precise value of Ω_f can in principle be determined from detailed computational fluid dynamics modeling or from experimental data and is not of immediate concern here. In the present work instead, we will focus only on the effects of such flows on the acoustic–structure interactions. When the disk vibrates, the fluid velocity field $\mathbf{u}$ is perturbed from its initial value:

$$\mathbf{u} = r\Omega_f \hat{\mathbf{e}}_\theta + \mathbf{u}', \tag{7}$$

where $\mathbf{u}'$ is the velocity perturbation of the flow from its initial bulk fluid rotation. The resulting acoustic equation governing the oscillations of the surrounding compressible fluid in the presence of rotating bulk fluid flow is written in nondimensional form as [33]

$$\nabla^2\phi = \frac{1}{C^2}\left(\frac{\partial}{\partial t} + \Omega_f \frac{\partial}{\partial \theta}\right)^2 \phi. \tag{8}$$

Towards subsequent computational analysis of the coupled equations (2) and (8) and the associated boundary conditions (5), it is convenient to cast the governing equations in a *fluid-fixed rotating frame*. In the fluid-fixed reference frame, Eq. (8) returns to the simple form of wave equation, Eq. (3), and the disk vibration equations take the form

$$w_{,tt} + 2\Omega^* w_{,t\theta} + \Omega^{*2} w_{,\theta\theta} + K_d[w] = \Lambda[[\phi_{,t}]]_{z=0}, \tag{9}$$

where Ω^* is the rotating speed of the disk relative to the fluid defined as

$$\Omega^* = \Omega - \Omega_f. \tag{10}$$

In addition, $K_d[\cdot]$ is the stiffness operator as defined in Eq. (4); however, it should be noted that the membrane stiffness terms, σ_r and σ_θ, in the stiffness operator remain functions of disk rotation speed Ω instead of the Ω^*.

In addition to the governing equations, it is important to verify the expressions for the boundary conditions (6) and the pressure loading (1) in the fluid-fixed rotating frame. First, the impermeability boundary conditions (6(a)) at the rigid wall are not influenced by the coordinate transformation. In addition, the velocity matching conditions (6(b)) on the disk surface and in the radial clearance remain unchanged. This is because the velocity potential, ϕ, and displacements, w and ζ, are defined in the same fluid-fixed coordinate system, and no additional convective terms arise in the associated boundary conditions.

2.3. Discretization of the coupled equations in the fluid-fixed rotating frame

In order to solve for the free vibrations of the coupled system, the system equations are discretized using the assumed modes method via Green's theorem. Accordingly, the fluid velocity potentials in the upper and lower enclosures, the transverse vibrations of the rotating disk, and the fluid velocity field on the artificial surface in the radial clearance are discretized using a set of mutually orthogonal, complete basis functions. These basis functions are, respectively, the rigid wall acoustic modes of the upper and lower enclosures, the in-vacuo stationary disk eigenfunctions, and the eigenfunctions of a free–free annular membrane

$$\phi^a(r,\theta,z;t) = \sum_n a_n(t) F_n^a(r,\theta,z), \tag{11a}$$

$$\phi^b(r,\theta,z;t) = \sum_n b_n(t) F_n^b(r,\theta,z), \tag{11b}$$

$$w(r,\theta;t) = \sum_m q_m(t)\psi_m(r,\theta), \tag{12}$$

$$\zeta(r,\theta;t) = \sum_r u_r(t)\varphi_r(r,\theta), \tag{13}$$

where a_n, b_n, u_r, q_m are, respectively, the generalized coordinates for the fluid potential in the upper, lower enclosures, and for the radial clearance and the rotating disk vibrations. $F_n^{a,b}$, ψ_m, and φ_r are, respectively, the acoustic normal modes of the upper and lower enclosures, the in vacuo disk modes of the stationary disk, and in vacuo annular membrane modes. The annular membrane modes are computed for uniformly tensioned membrane with free–free boundary conditions at the inner and the outer radii. The annular membrane modes are used to discretize the fluid motion in the radial clearance. Note that owing to the axisymmetry of the geometry, each asymmetric basis function is divided into sine and cosine components, and the sine and cosine components are denoted in the text and appendices by the superscripts S and C, respectively.

The discretized equations of disk vibrations are derived in the *fluid-fixed rotating frame*. Application of the above discretization to Eq. (9) yields for the disk vibration

$$\ddot{q}_m^C + 2m_1\Omega^*\dot{q}_m^S + k_m q_m^C = \Lambda A_d\left(\sum_n \dot{a}_n^C L_{nm}^{aC} - \sum_n \dot{b}_n^C L_{nm}^{bC}\right), \tag{14a}$$

$$\ddot{q}_m^S - 2m_1\Omega^*\dot{q}_m^C + k_m q_m^S = \Lambda A_d\left(\sum_n \dot{a}_n^S L_{nm}^{aS} - \sum_n \dot{b}_n^S L_{nm}^{bS}\right), \tag{14b}$$

where k_m are elements representing disk bending and membrane stiffness [16]. Note that L_{nm} indicates acoustic–structure coupling coefficients defined by the inner product between acoustic normal modes and in vacuo disk modes over the disk surface, and are evaluated separately for the upper- and lower-enclosure sine

and cosine modes, i.e.,

$$L_{nm}^{a,b} = \frac{1}{A_d}\int_{A_d} F_n^{a,b}\psi_m \,\mathrm{d}A. \tag{15}$$

In contrast to the disk equations, the basis functions for the acoustic fields do not satisfy boundary conditions (6). In fact, it is not possible to choose a set of comparison functions satisfying all the acoustic boundary conditions, not only because of the complexity of the boundary conditions but also because of the coupling with disk vibrations. For these reasons, we adopt Green's Theorem used routinely in acoustic–structure coupling problems [34,35]. Further, by the application of the boundary conditions, the acoustic governing equation for upper enclosure in the fluid-fixed reference frame can be written as [16]

$$\frac{1}{C^2}\int_{V^a}[F_n^a\ddot{\phi}^a + (\Lambda_n^a)^2\phi^a F_n^a]\,\mathrm{d}V = -\int_{A_d} F_n^a\dot{w}\,\mathrm{d}A - \int_{A_u} F_n^a\dot{\zeta}\,\mathrm{d}A, \tag{16}$$

where the dot denotes temporal differentiation. The equation for the lower enclosure has the same form as Eq. (16), except with a positive sign on the right-hand side due to the opposite direction of the normal vectors. These can be regarded as weak forms of the original governing equation (3). Indeed, because exact comparison functions were not used for the acoustic oscillations, it is expected that the resulting solution does not converge pointwise to the correct boundary normal velocity. However, it is expected that this solution converge correctly to the surface pressure, which is needed for the correct formulation of the coupled equation [35]. Substituting Eqs. (11)–(13) into Eq. (16) with the assistance of the orthogonality yields the discretized equations for the velocity potentials coupled to the disk vibration

$$\frac{V^a M_n^a}{C^2}\left[\ddot{a}_n + (\Lambda_n^{\leftrightarrows a})^2 a_n\right] = -A_d\sum_m \dot{q}_m L_{nm}^a - A_u\sum_r \dot{u}_r N_{nr}^a, \tag{17}$$

where

$$N_{nr}^{a,b} = \frac{1}{A_u}\int_{A_u} F_n^{a,b}\varphi_r \,\mathrm{d}A \tag{18}$$

are the radial clearance induced inter-cavity coupling coefficients. Note that Eq. (18) is composed of sine and cosine modes, and N_{nr} is evaluated separately for the upper- and lower-enclosure sine and cosine modes.

It is interesting to note that the coupled equations (14) and (17) are indeterminate in the sense that there are more degrees of freedom than the number of equations. To address this indeterminacy, the continuity of the acoustic pressure across the radial clearance needs to be satisfied [34,36]

$$\dot{\phi}^a = \dot{\phi}^b \text{ on } A_u. \tag{19}$$

Multiplying through by φ_r after substituting Eq. (11) into Eq. (19), and integrating over A_u gives

$$\sum_{n=0}\dot{a}_n N_{nr}^a = \sum_{n=0}\dot{b}_n N_{nr}^b. \tag{20}$$

This yields the constraint equations that must be satisfied along with the coupled discretized equations (14) and (17). In the context of the variational formulation, u_r may be regarded as Lagrange multipliers because they enforce the continuity constraint of acoustic pressures between upper and lower enclosures. Therefore, the present analysis can also be thought of as a component mode synthesis where the components are individual enclosures [34]. Furthermore, the relationship in Eq. (20) yields the same result as using the Green's function approach [36]. Finally, these are holonomic constraints [37].

Combining Eqs. (14) and (17) with Eq. (20) yields the gyroscopically coupled discretized equations with holonomic constraints that govern the flexible disk vibrations rotating in an enclosed compressible fluid in the

presence of a radial clearance and rotating bulk fluid flow. In the *fluid-fixed rotating frame*,

$$\begin{bmatrix} \mathbf{M}_a & & & \\ & \mathbf{M}_b & & \\ & & \mathbf{M}_q & \\ & & & \mathbf{0} \end{bmatrix} \begin{Bmatrix} \ddot{a}_n \\ \ddot{b}_n \\ \ddot{q}_m \\ \ddot{u}_r \end{Bmatrix} + \begin{bmatrix} & & \mathbf{L}_{aq} & \mathbf{N}_{au} \\ & & -\mathbf{L}_{bq} & -\mathbf{N}_{bu} \\ -\mathbf{L}_{aq}^{\mathrm{T}} & \mathbf{L}_{bq}^{\mathrm{T}} & \mathbf{G}_q & \\ -\mathbf{N}_{au}^{T} & \mathbf{N}_{bu}^{T} & & \end{bmatrix} \begin{Bmatrix} \dot{a}_n \\ \dot{b}_n \\ \dot{q}_m \\ \dot{u}_r \end{Bmatrix} + \begin{bmatrix} \mathbf{K}_a & & & \\ & \mathbf{K}_b & & \\ & & \mathbf{K}_q & \\ & & & \mathbf{0} \end{bmatrix} \begin{Bmatrix} a_n \\ b_n \\ q_m \\ u_r \end{Bmatrix} = \mathbf{0}. \tag{21}$$

The components of the above submatrices are given in Appendix A. The mass and stiffness matrices are each composed of diagonal block matrices of upper, lower enclosures, rotating disk and membrane for a radial clearance. Several characteristics of the coupled system in Eq. (21) are listed below:

(1) The system has the form of a classical discretized gyroscopic system. Due to the zero "mass" associated with the generalized coordinates in the radial clearance, however, this system leads to a rank-deficient singular eigenvalue problem. In the next section, a method will be introduced to remove this singularity to reduce this to the form of a standard gyroscopic system without singularities.
(2) The system features three intrinsically different gyroscopic effects: ($\mathbf{L}_{aq}$, $\mathbf{L}_{bq}$) describes the gyroscopic coupling between the disk vibrations and upper- and lower-enclosure acoustic oscillations. Similarly, ($\mathbf{N}_{au}$, $\mathbf{N}_{bu}$) describe the gyroscopic coupling through the radial clearance of the upper- and lower-enclosure acoustic oscillations. Finally $\mathbf{G}_q$ is the gyroscopic coupling due to the disk rotation.
(3) The vanishing natural frequency of the fundamental acoustic mode renders positive the semi-definite system stiffness matrix. However, the elimination of singular terms due to the radial clearance generates nonzero terms in the fundamental acoustic mode (see Section 3). Consequently, this process ensures the stiffness matrix is invertible, and leads to the Helmholtz stiffening effect in a similar manner as in Ref. [38].
(4) The system equations here allow for different air gaps in the upper and lower enclosures, i.e., $L^a \neq L^b$. For a symmetrically positioned disk, all submatrices representing upper and lower enclosures become identical.

In what follows, we will investigate computationally the discretized dynamical system (21), while focusing in sequence on the effects on the acoustic–structure interaction and coupled system instabilities of (a) radial clearance, (b) asymmetric disk positioning, (c) rotating bulk fluid flows, and (d) disk, acoustic and fluid dampings.

3. Effects of radial clearance

We consider first the case where a radial clearance is present while the disk is positioned symmetrically in the enclosure and the surrounding fluid is initially stationary.

3.1. Derivation of reduced coupled discretized equations

As pointed out in Section 2, Eq. (21) is in the form of a singular eigenvalue problem due to the zero mass terms of the radial clearance region. From a mathematical point of view, this problem falls into the category of a singular case of generalized non-Hermitian eigenvalue problem (GNHEP). Such problems are numerically challenging in the sense that arbitrarily small perturbations may change the eigenvalues completely [39]. In general, the QZ algorithm is not capable of handling this type of problem in a reliable way, and only a limited number of numerical algorithms have been developed for this problem. For example, Generalized UPper TRIangular (GUPTRI) algorithm computes a generalization of the Schur canonical form to matrix pairs.

However, because this algorithm generates Jordan structures, which are not stable in numerical computation, it is not capable of solving the coupled eigenvalue problems with large condition numbers. Therefore, we adopt a different scheme to solve this eigenvalue problem.

First, we simplify the problem considering identical upper and lower enclosures, and when $n_1 \neq 0$, as an example. In this case, because $L^a = L^b$, if we choose same sets of basis functions for upper and lower enclosures, the coupling terms become identical. Furthermore, the mass and stiffness terms of the upper and lower enclosures are identical. Therefore, the corresponding problem becomes, in terms of the unknown eigenvalues ω,

$$\begin{bmatrix} \mathbf{K}_{nm} - \omega^2 \mathbf{M}_{nn} & & \omega \mathbf{L}_{nm} & \omega \mathbf{N}_{nr} \\ & \mathbf{K}_{nn} - \omega^2 \mathbf{M}_{nn} & -\omega \mathbf{L}_{nm} & -\omega \mathbf{N}_{nr} \\ -\omega \mathbf{L}_{nm}^{\mathrm{T}} & \omega \mathbf{L}_{nm}^{\mathrm{T}} & \mathbf{K}_q + \omega \mathbf{G}_q - \omega^2 \mathbf{M}_q & \\ -\omega \mathbf{N}_{nr}^{\mathrm{T}} & \omega \mathbf{N}_{nr}^{\mathrm{T}} & & \mathbf{0} \end{bmatrix} \begin{Bmatrix} a_n \\ b_n \\ q_m \\ u_r \end{Bmatrix} = 0. \tag{22}$$

Secondly, introducing several steps of row and column operations, it can be shown that the above matrix identically simplifies to

$$\left[\begin{array}{c|ccc} \mathbf{K}_{nn} - \omega^2 \mathbf{M}_{nn} & & & \\ \hline & \mathbf{K}_{nn} - \omega^2 \mathbf{M}_{nn} & -2\omega \mathbf{L}_{nm} & -2\omega \mathbf{N}_{nr} \\ & \omega \mathbf{L}_{nm}^{\mathrm{T}} & \mathbf{K}_q + \omega \mathbf{G}_q - \omega^2 \mathbf{M}_q & \\ & \omega \mathbf{N}_{nr}^{\mathrm{T}} & & \mathbf{0} \end{array}\right] \begin{Bmatrix} a_n + b_n \\ b_n - a_n \\ q_m \\ u_r \end{Bmatrix} = 0. \tag{23}$$

It is interesting to note that the entire matrix is separated into two diagonal block matrices. Because the determinant of the entire matrix is the product of the determinant of each block matrix, the eigenvalues of the entire system are composed of the eigenvalues of the block matrices. From this it is clear that all eigenvalues of the upper block matrix are identical to those of uncoupled acoustic enclosure. This shows explicitly that there exist acoustic modes that are uncoupled from disk vibration, even in the presence of a radial clearance. These are also called *in-phase* acoustic modes because the acoustic pressure in the upper and lower cavities oscillates in-phase in these modes. On the other hand, the acoustic modes that couple to disk vibrations are called the *out-of-phase* modes, wherein the acoustic pressure in the upper and lower enclosures oscillate out-of-phase.

Now, in order to find the coupled acoustic and disk modes, we need to find the roots of the characteristic equation from the lower block matrix. However, the lower block matrix is still singular and it is not possible to solve for the roots using standard eigenvalue solvers yet. To overcome this problem, we transform the singular GNHEP to a regular problem by eliminating the singular terms. In fact, the last row equations in Eq. (23) act as kinematic constraints to the other equations, and arise out of the acoustic pressure continuity equations in the radial clearance. Therefore, we split the unconstrained generalized coordinates b_n^* and $\mathbf{N}_{nr}$ into two parts, i.e.,

$$b_n^* = \begin{Bmatrix} b_c^* \\ b_u^* \end{Bmatrix}_n \quad \text{and} \quad \mathbf{N}_{nr} = \begin{bmatrix} \mathbf{N}_c \\ \mathbf{N}_u \end{bmatrix}_{nr}, \tag{24}$$

where the generalized coordinates selected for elimination are the constrained variables, b_c^* [40]. Further, defining the transformation matrix, $\mathbf{T}$, such that

$$b_n^* = \mathbf{T} \cdot b_u^* \quad \text{where} \quad \mathbf{T} = \begin{bmatrix} -\mathbf{N}_c^{-\mathrm{T}} \mathbf{N}_u^{\mathrm{T}} \\ \mathbf{1} \end{bmatrix}, \tag{25}$$

we can derive reduced coupled equations of the problem (see Appendix B for details). That is,

$$\begin{bmatrix} \mathbf{T}^{\mathrm{T}} \mathbf{M}_{nn} \mathbf{T} & \\ & 2\mathbf{M}_q \end{bmatrix} \begin{Bmatrix} \ddot{b}_u^* \\ \ddot{q}_m^* \end{Bmatrix} + 2 \begin{bmatrix} & -\mathbf{T}^{\mathrm{T}} \mathbf{L}_{nm} \\ (\mathbf{T}^{\mathrm{T}} \mathbf{L}_{nm})^{\mathrm{T}} & \mathbf{G}_q \end{bmatrix} \begin{Bmatrix} \dot{b}_u^* \\ \dot{q}_m^* \end{Bmatrix} + \begin{bmatrix} \mathbf{T}^{\mathrm{T}} \mathbf{K}_{nn} \mathbf{T} & \\ & 2\mathbf{K}_q \end{bmatrix} \begin{Bmatrix} b_u^* \\ q_m^* \end{Bmatrix} = 0. \tag{26}$$

Clearly, the reduced discretized equation (26) still has the form of a gyroscopic system without singularities. In addition, the artificial coordinates, $\boldsymbol{u}_r$, used for the radial clearance have been eliminated in the reduced coupled equation. Note, however, the inter-cavity coupling terms $\mathbf{N}_{nr}$ between the upper and lower enclosures are still retained and are embedded in other submatrices. Finally, the dimension of the reduced equations is smaller than the original equation so that eigenvalues can be calculated efficiently.

3.2. Computational issues and convergence study

Several numerical techniques are used to ensure accurate and fast computations. First, the coupling terms ($\mathbf{L}_{nm}$ and $\mathbf{N}_{nr}$) are defined through inner products with circumferentially harmonic disk and membrane basis functions. Therefore, disk and upper- and lower-enclosure acoustic modes couple only if their nodal diameters are equal. Accordingly, the entire set of coupled equations can be divided conveniently into separate sets of coupled equations depending on the nodal diameter number of the basis functions. For a specific nodal

Table 1
Dimensions and mechanical properties of the disk and acoustic enclosure used in computations

Variables	Data	Physical meaning
R_o	4.74 cm	Outer radius of the disk
R_i	1.56 cm	Inner radius of the disk
R_w	4.94 cm	Outer radius of the enclosure
H	0.790 mm	Disk thickness
ρ_d	2700 kg/m^3	Disk density
ρ_f	1.2 kg/m^3	Air density
E	71 GPa	Young's modulus of the disk
v	0.33	Poisson's ratio of the disk
c_o	343 m/s	Speed of sound in air

These parameters correspond approximately to those of a hard-disk drive platter.
Note: In the absence of the radial clearance, outer radius of the enclosure is replaced by that of the disk.

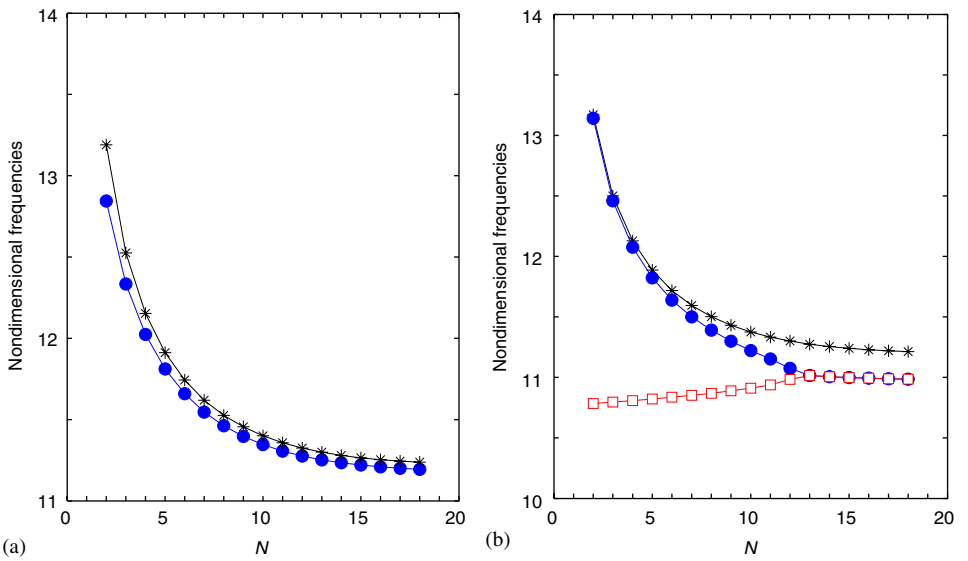

Fig. 3. Convergence characteristics of the three nodal diameter modes in the presence of a radial clearance: (a) at just below critical speed ($\Omega = 50$) and (b) at just below mode coalescence speed ($\Omega = 600$): ●, $(3,0,0)_{\mathrm{B}}^{\mathrm{out}}$; *, $(3,0,0)_{\mathrm{F}}^{\mathrm{out}}$; □, $(3,0)_{\mathrm{R}}$. This computation is performed for the undamped system, with system parameters listed in Table 1 and 1 cm air gaps are chosen for the computation. Each N corresponds to the use of N disk modes and $2N^2$ acoustic modes in the computation, when $N_{\mathrm{membrane}} = 1$.

diameter number, the original dimension of the discretized system in state space is $2(2N^3 + N^2 + N^2_{\text{membrane}})$. However, upon the elimination of the singular terms caused by a radial clearance, the size of the system matrix reduces to $2\{2(N - N_{\text{membrane}})^2 + N\}$. Here, N stands for the number of basis functions of the disk and enclosure in each direction, and N_{membrane} stands for the number of annular membrane basis functions. This numerical scheme allows for effective and separate computations for each family of nodal diameter number modes. For these reasons, in this study, each family of nodal diameter modes is calculated independently based on system parameters listed in Table 1. The data in Table 1 correspond approximately to those of a commercial hard disk drive.

To investigate acoustic–structure coupling and the onset of flutter accurately, detailed convergence characteristics of the discretized system are also studied. Fig. 3 shows some key convergence characteristics of three nodal diameter modes to highlight interesting features of this eigenvalue problem in the presence of a radial clearance. The subscripts R, B, and F indicate reflected, backward, and forward traveling waves (RTWs, BTWs, FTWs), respectively. For a specific nodal diameter mode, each $\boldsymbol{N}$ corresponds to the use of N disk modes and $2N^2$ acoustic modes in the computation, when $N_{\text{membrane}} = 1$. For comparison, two different rotating speeds are chosen such that Fig. 3(a) is just below critical speed ($\Omega = 50$), and Fig. 3(b) is just below speed for mode coalescence ($\Omega = 600$). In Fig. 3, the computations are performed using one membrane basis

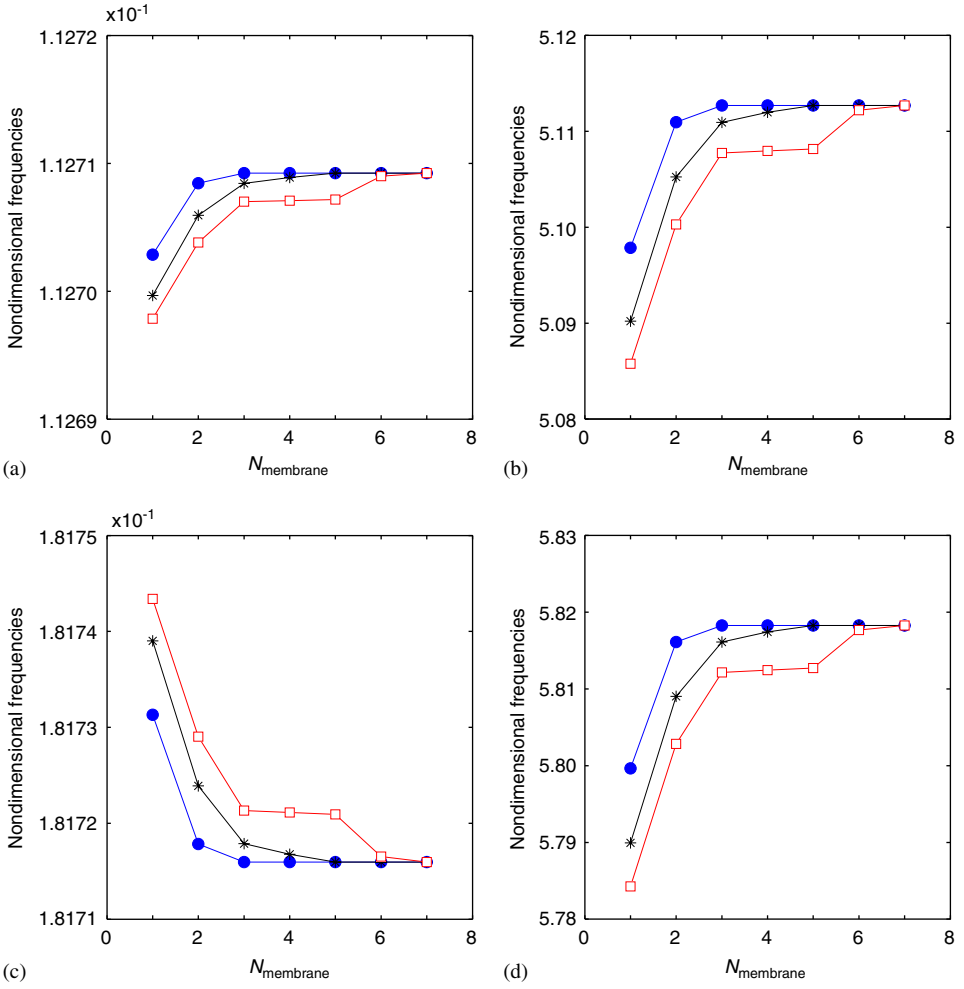

Fig. 4. Convergence characteristics of three nodal diameter modes with respect to the number of basis functions used for the radial clearance: (a) $(3,0)_B$ at subcritical speed ($\Omega = 50$), (b) $(3,0)_F$ at subcritical speed ($\Omega = 50$), (c) $(3,0)_B$ at supercritical speed ($\Omega = 60$), and (d) $(3,0)_F$ at supercritical speed ($\Omega = 60$). ●, $N = 3$; *, $N = 5$; □, $N = 7$.

function. The frequencies of the out-of-phase acoustic-dominated modes converge from above at subcritical speeds as the number of basis functions increase, because the stiffness matrices are positive definite [41]. Beyond the critical speed, however, the frequencies of (3,0) RTW converge from below, as reported in Ref. [42].

Interestingly, the eigenvalues computed using different numbers of annular membrane basis functions used in the radial clearance show different convergence characteristics. Fig. 4 shows the eigenvalues of the coupled three nodal diameter modes at sub- and supercritical speeds with respect to the number of annular membrane basis functions. Three different cases, when $N = 3$, 5, and 7, are chosen to confirm the dependency of the number of disk and acoustic modes. According to the results, all eigenvalues converge from below at subcritical speed range, as the number of membrane basis functions is increased. Further, beyond the critical speed (Fig. 4(b)), the frequencies of disk-dominated RTW converge from above. Based on these convergence studies on the annular membrane basis functions used in the radial clearance, only one membrane basis function is used in all subsequent calculations. A choice of $N_{\text{membrane}} = 1$ shows the prediction to within 1.5% of the asymptotic value of the (3,0) RTW disk-dominated mode frequencies at $\Omega = 600$. Note however that larger radial clearances may require more membrane basis functions for convergence. In addition, we choose at least $N = 5$ (or 56 basis functions for each family of mode with the same nodal diameter number) in the computations in order to ensure sufficient accuracy.

Following this convergence study, the physics of acoustic–structure interaction in the presence of radial clearance is investigated.

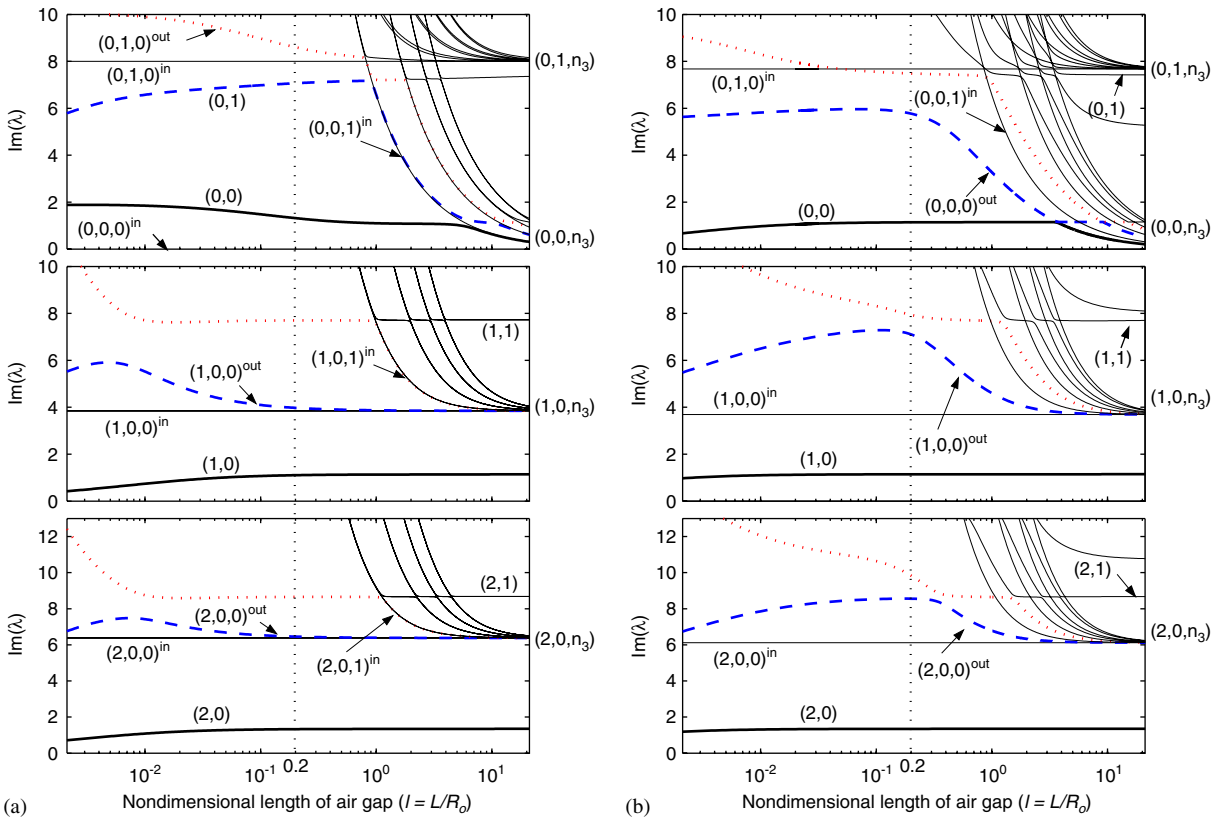

Fig. 5. Coupled natural frequencies as a function of nondimensional length of air gap, l, in the presence of a radial clearance, when the disk is stationary in a cylindrical enclosure: (a) in the absence of radial clearance, (b) in the presence of radial clearance. This computation is performed for the stationary disk with system parameters listed in Table 1.

3.3. Acoustic–structure interactions of enclosure with stationary disk

Because the disk and acoustic oscillation equations are coupled, it is expected that the system modes will be no longer purely structural or purely acoustic. For most cases, a system mode will be referred to as acoustic-dominated or disk-dominated depending on the relative contributions of disk or acoustic oscillations to the mode in question. This question is studied more quantitatively for a stationary disk in this subsection and the influence of radial and axial air gaps on the physics of acoustic–structure coupling is also explored. The coupled system frequencies of the zero to three nodal diameter modes with respect to the nondimensional length of the axial air gap, l, are shown in Fig. 5 for the parameters described in Table 1. To highlight the effects of the radial clearance, the frequencies in the absence of radial clearance are also shown in Fig. 5(a), which are the same results as in Ref. [16]. Note that the radius of the enclosure in the presence of radial clearance is slightly larger (2 mm) than that of the enclosure with no radial clearance.

From Fig. 5, several effects can be observed of the radial clearance on the coupled eigenvalues of the system. First, in the absence of radial clearance, the (0,0,0) acoustic mode has zero frequency. However, as soon as a radial clearance is included, the (0,0,0) acoustic mode oscillations in the top and bottom enclosures couple through the radial clearance leading to a nonzero frequency of the (0,0,0) out-of-phase acoustic mode. In fact, the frequency of any out-of-phase acoustic mode increases as soon as a radial clearance is included. This occurs because in the absence of radial clearance, upper- and lower-enclosure acoustic modes couple only through disk vibrations. Once a radial clearance is included, the inter-acoustic coupling in the radial clearance increases the overall coupling between the upper and lower cavity acoustic modes. Consequently, the strain energy of the out-of-phase modes and therefore their natural frequencies increase once a radial clearance is included.

Secondly, in the presence of radial clearance, eigenvalue veering occurs between (0,1) disk-dominated and (0,0,0) out-of-phase acoustic-dominated modes in the range of l from 0.2 to 10. Because these modes are coupled, it is only expected that eigenvalue veering occurs when their uncoupled frequencies come close to each other. In comparison, because they are decoupled no veering occurs between (0,0) disk-dominated and (0,0,n_3) in-phase acoustic-dominated modes.

Thirdly, the frequency of the (0,0) disk-dominated mode decreases as the axial air gap decreases. This is in contrast to the case of no radial clearance. Instead of the added stiffness effect due to the Helmholtz stiffening effect in the absence of radial clearance, inter-acoustic coupling through the radial clearance acts as an added mass on this mode.

Finally, similar phenomena are encountered for the asymmetric modes as well. Out-of-phase acoustic modes exist as they do for axisymmetric modes, and several eigenvalue veering phenomena occur with changing axial gap length. Interestingly, in the presence of radial clearance, the eigenvalue veering occurs at a larger air gap than in the absence of radial clearance. Note that 1 cm axial air gap used in these calculations corresponds to $l = 0.2$ in Figs. 5 and 6. Therefore, acoustic–structure eigenvalue veering can be a realistic concern in commercial hard disk drives.

The presence of eigenvalue veering in such coupled structure–acoustic systems is important because small changes in system parameters can lead to the sudden change of a structure-dominated mode into an acoustic-dominated mode and vice versa. Accordingly, the extent of acoustic coupling in a mode as measured by the ratio of acoustic energy to the total energy in that mode can be analyzed using the ratio of acoustic to total strain energy in the oscillation mode. This ratio, Γ, is defined as

$$\Gamma = \frac{\bar{\mathbf{\Phi}}_A^{\mathrm{T}} \mathbf{K}_A \mathbf{\Phi}_A}{\bar{\mathbf{\Phi}}_A^{\mathrm{T}} \mathbf{K}_A \mathbf{\Phi}_A + \bar{\mathbf{\Phi}}_q^{\mathrm{T}} \mathbf{K}_q \mathbf{\Phi}_q}, \tag{27}$$

where $\mathbf{K}_A$ and $\mathbf{K}_q$ indicate stiffness matrices of acoustic enclosures (upper and lower) and the stationary disk, respectively, In addition, $\mathbf{\Phi}_A$ and $\mathbf{\Phi}_q$ are the corresponding eigenvectors of acoustic and disk oscillations, and a bar denotes complex conjugate of the eigenvectors. The percentage Γ in the zero to three nodal diameter modes of the coupled system as a function of nondimensional length of axial air gap is illustrated in Fig. 6. For comparison, these results are calculated in the absence of radial clearance also as before. Note that at large air

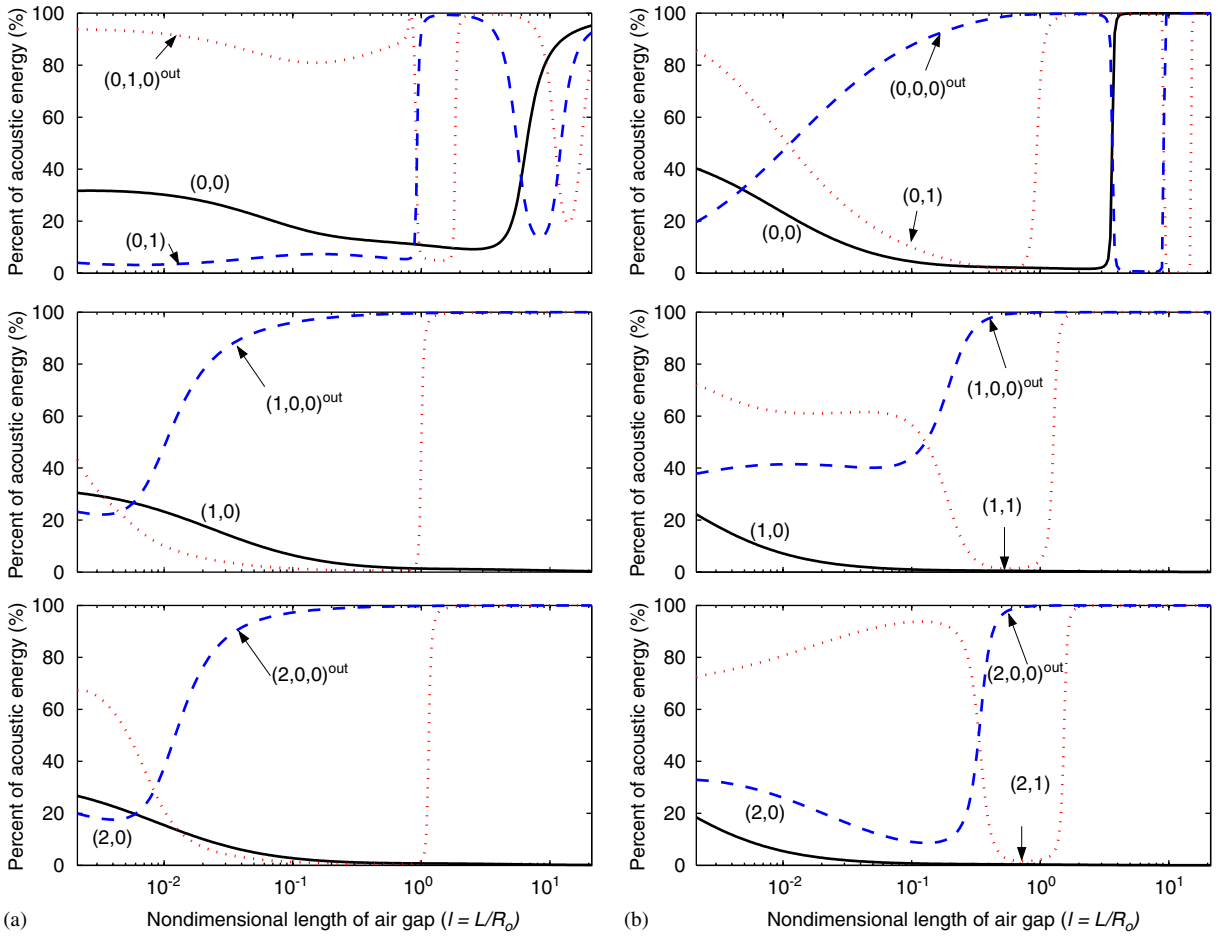

Fig. 6. Percent of acoustic energy to the total energy in mode in the presence of a radial clearance, when the disk is stationary in a cylindrical enclosure: (a) in the absence of radial clearance, (b) in the presence of radial clearance.

gaps, sudden changes of acoustic energy occur due to the eigenvalue veering phenomena. As the air gap is decreased, the disk modes become truly acoustic–structural with a significant component of vibrations stored as acoustic oscillations in the enclosure. For example, nearly 20% of the energy of the (0,0) mode at a nondimensional air gap of 10^{-2} is stored in the acoustic field. The results indicate that structural–acoustic interactions are quite significant in modifying the mode shapes of the structure especially at small gap widths. The results also imply that small form factor disk drives like a micro-drive may involve significant structure acoustic interactions. Such eigenvalue veering phenomena are not only important in the design of low-noise rotating disk systems but also for understanding the onset of certain types of aeroelastic instabilities of the rotating disk.

In addition to the length of axial air gap, the extent of radial clearance also affects significantly the acoustic–structure interaction. The coupled frequencies of three nodal diameter modes versus the nondimensional length of radial clearance, R_o/R_w, are illustrated in Fig. 7, where solid and dotted lines indicate the cases with and without ($\mathbf{L}_{nm} = 0$) acoustic–structure coupling, respectively. The same parameters in Table 1 and 1 cm axial air gap were used for the computations; however, the outer disk radius R_o is decreased. An eigenvalue veering is observed between the (3,0) disk-dominated and (3,0,0) out-of-phase acoustic-dominated modes. These results indicate that the radial clearance can also be used as a sensitive design parameter to alter acoustic–structure interactions in enclosed rotating disk systems.

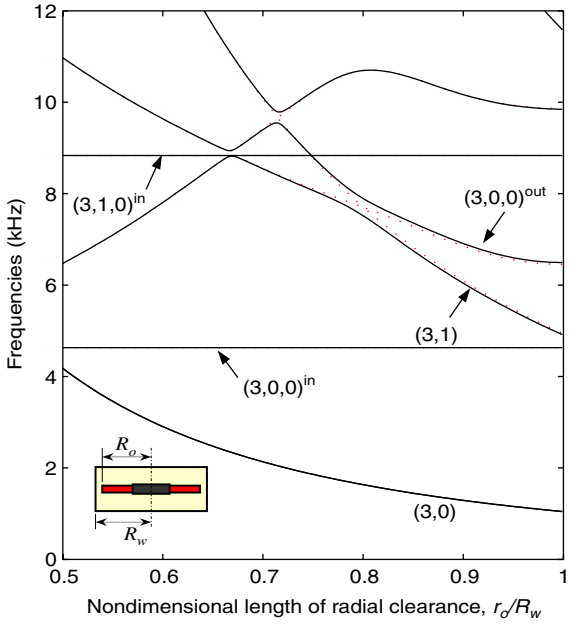

Fig. 7. Coupled frequencies of three nodal diameter modes versus nondimensional length of radial clearance, R_o/R_w, where solid and dotted lines indicate the case of with and without ($\mathbf{L}_{nm} = 0$) acoustic–structure couplings, respectively. Except the outer radius of the disk, the same parameters in Table 1 and 1 cm air gap were used for this computation.

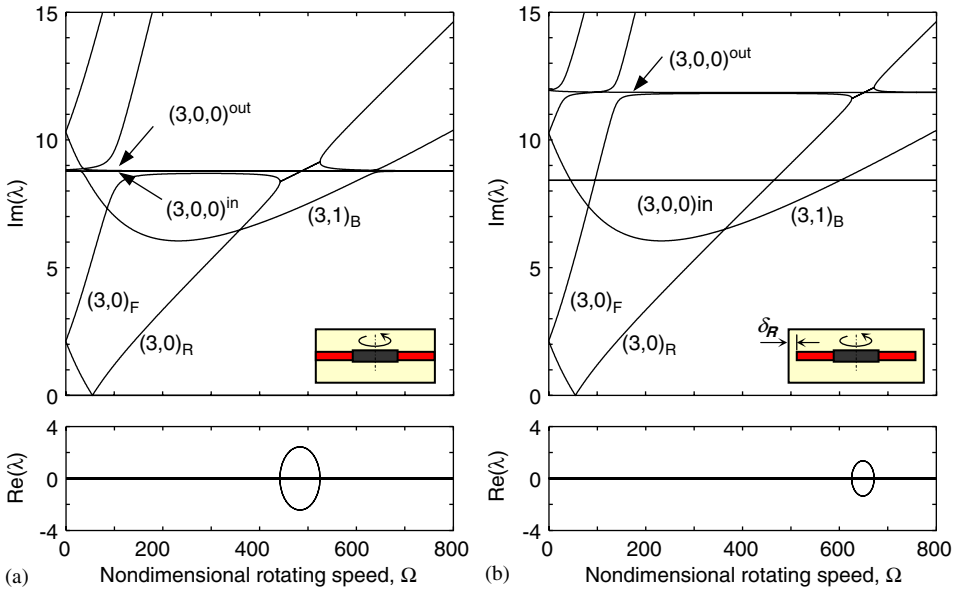

Fig. 8. Coupled eigenvalues of three nodal diameter modes without and with a radial clearance in the absence of rotating base flow: (a) without radial clearance, (b) with radial clearance. This computation is performed for the undamped system, with the system parameters listed in Table 1, and 1 cm air gap and 2 mm radial clearance are chosen for the computation.

3.4. Acoustic–structure interactions of enclosure with rotating disk

The eigenvalues of the coupled system in the presence of disk rotation are now investigated. Fig. 8 shows several new effects arising out of the presence of the radial clearance. First, at zero rotation speed, the

frequency of the (3,0,0) out-of-phase acoustic mode increases by nearly 35% while that of the (3,0,0) in-phase acoustic mode remains unchanged in the presence of the radial clearance. The small decrease in the frequency of the in-phase acoustic mode is because the radius of enclosure is increased a little by the amount of the radial clearance (2 mm). Secondly, the effect of a radial clearance on the flutter speed is of particular interest. While the disk critical speeds remain unchanged, the disk-dominated FTW veers with the (3,0,0) out-of-phase acoustic modes at a much higher rotation speed as compared to the case of no radial clearance. This is a direct consequence of the high out-of-phase acoustic mode frequency. Finally, in the absence of damping, the three nodal diameter modes destabilize via a flutter instability arising from mode coalescence. The flutter speed is higher and the speed range of instability is smaller in the presence of the radial clearance.

In summary, the presence of a small radial clearance increases significantly the out-of-phase acoustic mode frequency, increases the speed at which flutter due to mode coalescence occurs, and decreases the speed range of this instability. The effects of disk and acoustic damping are basically the same as the case of the damped system without a radial clearance, and will be discussed in Section 6.

4. Effect of asymmetric positioning

The effects of another geometric perturbation are now considered with $L^a \neq L^b$ so that the disk is asymmetrically positioned in the enclosure. Radial clearance and rotating base flows are neglected to focus on the effects of disk positioning in the enclosure.

4.1. Existence of in-phase acoustic modes

Clearly, if the air gaps above and below the disks are different, certain symmetries of the coupled eigenvalue problem will change. In fact, it is not at all clear whether the in-phase and out-of-phase acoustic modes continue to exist in the presence of such asymmetry. However, the existence of in-phase acoustic modes can be proven mathematically even in the case of asymmetric positioning. The key idea of this proof is through the use of matrix partitioning. If the upper and lower enclosures have the same diameters, the acoustic modes in the upper and lower enclosures with zero z-directional modes $(n_1, n_2, 0)$ are identical. This implies that both upper and lower enclsoures have several common elements in mass and stiffness matrices corresponding to the zero z-directional modes. Therefore, because both mass and stiffness matrices are diagonal, it is possible to split acoustic mass and stiffness matrices into two submatrices; one is identical and common to both enclosures and the other represents different matrices corresponding to higher z-directional acoustic modes that are distinct for the upper and lower enclosures, i.e.,

$$\mathbf{M}_{a,b} = \begin{bmatrix} \tilde{\mathbf{M}} & \\ & \hat{\mathbf{M}}_{a,b} \end{bmatrix} \quad \text{and} \quad \mathbf{K}_{a,b} = \begin{bmatrix} \tilde{\mathbf{K}} & \\ & \hat{\mathbf{K}}_{a,b} \end{bmatrix}, \tag{28}$$

where the symbols tilde ($\sim$) and hat ($\wedge$) indicate the common and distinct submatrices, respectively, of upper and lower enclosures. Furthermore, because the coupling coefficients, $\mathbf{L}_{nm}$, are calculated over the disk surface ($z = 0$), they are independent of the number of z-directional modes. In other words, the coupling coefficients, $\mathbf{L}_{nm}$, of upper and lower enclosures are identical, as long as we choose the same family of basis functions for them. Then, following immediately from the same idea as before, it is possible to split the coupling matrix into two submatrices, i.e.,

$$\mathbf{L}_{nm}^a = \mathbf{L}_{nm}^b = \mathbf{L}_{nm} = \begin{bmatrix} \tilde{\mathbf{L}}_{nm} & \\ & \hat{\mathbf{L}}_{nm} \end{bmatrix}. \tag{29}$$

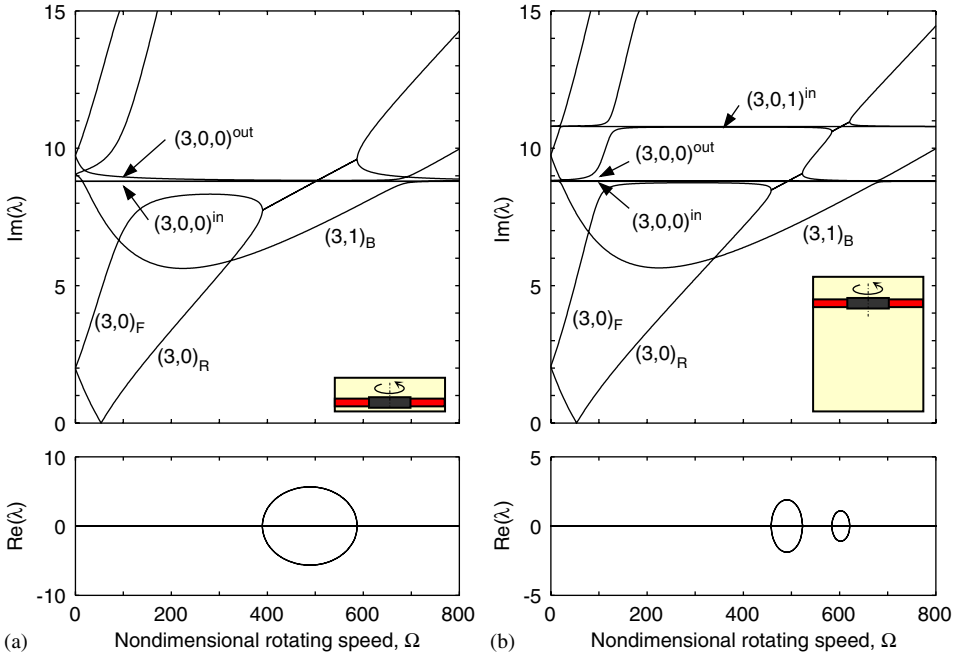

Fig. 9. Three nodal diameter coupled eigenvalues of an asymmetrically placed disk in an enclosure with small and large air gaps in the z-direction: (a) when $L^a = 1\,\text{cm}$ and $L^b = 0.1\,\text{cm}$, (b) when $L^a = 1\,\text{cm}$ and $L^b = 5\,\text{cm}$. This computation is performed in the absence of dissipation or rotating base flow, using the system parameters listed in Table 1.

Substituting Eqs. (28) and (29) into Eq. (22) in the absence of radial clearance leads to the following eigenvalue problem:

$$\begin{vmatrix} \tilde{\mathbf{K}} - \omega^2\tilde{\mathbf{M}} & & & & \omega\tilde{\mathbf{L}}_{nm} \\ & \hat{\mathbf{K}}_a - \omega^2\hat{\mathbf{M}}_a & & & \omega\hat{\mathbf{L}}_{nm} \\ & & \tilde{\mathbf{K}} - \omega^2\tilde{\mathbf{M}} & & -\omega\tilde{\mathbf{L}}_{nm} \\ & & & \hat{\mathbf{K}}_b - \omega^2\hat{\mathbf{M}}_b & -\omega\hat{\mathbf{L}}_{nm} \\ -\omega\tilde{\mathbf{L}}_{nm}^{\mathrm{T}} & -\omega\hat{\mathbf{L}}_{nm}^{\mathrm{T}} & \omega\tilde{\mathbf{L}}_{nm}^{\mathrm{T}} & \omega\hat{\mathbf{L}}_{nm}^{\mathrm{T}} & \mathbf{K}_q + \omega\mathbf{G}_q - \omega^2\mathbf{M}_q \end{vmatrix} = \mathbf{0}. \tag{30}$$

Further, utililizing row and column operations, as shown in the previous section, leads to two diagonal block matrix equations, i.e.,

$$\left|\begin{array}{c|cccc} \tilde{\mathbf{K}} - \omega^2\tilde{\mathbf{M}} & \mathbf{0} & \mathbf{0} & \mathbf{0} & \mathbf{0} \\ \hline \mathbf{0} & \hat{\mathbf{K}}_a - \omega^2\hat{\mathbf{M}}_a & & & \omega\hat{\mathbf{L}}_{nm} \\ \mathbf{0} & & \tilde{\mathbf{K}} - \omega^2\tilde{\mathbf{M}} & & -2\omega\tilde{\mathbf{L}}_{nm} \\ \mathbf{0} & & & \hat{\mathbf{K}}_b - \omega^2\hat{\mathbf{M}}_b & -\omega\hat{\mathbf{L}}_{nm} \\ \mathbf{0} & -\omega\hat{\mathbf{L}}_{nm}^{\mathrm{T}} & \omega\tilde{\mathbf{L}}_{nm}^{\mathrm{T}} & \omega\hat{\mathbf{L}}_{nm}^{\mathrm{T}} & \mathbf{K}_q + \omega\mathbf{G}_q - \omega^2\mathbf{M}_q \end{array}\right| = \mathbf{0}. \tag{31}$$

Clearly, the above equation shows that the entire system matrix is composed of uncoupled and coupled subsystems. The corresponding eigenvalues are, respectively, those of the in-phase and out-of-phase modes. Even if a radial clearance is present in the system, the same process is applicable because the coupling coefficients, $\mathbf{N}_{nr}$, have the same properties as $\mathbf{L}_{nm}$.

4.2. Computational results

Coupled eigenvalues of three nodal diameter modes are calculated as a function of nondimensionalized rotating speed, for disk parameters listed in Table 1. Fig. 9 illustrates two different situations; 0.1 and 1 cm air gaps in the lower and upper enclosures, and 5 and 1 cm air gaps in the lower and upper enclosures. Based on the computational results in Fig. 9, several effects of asymmetric positioning can be deduced.

(1) The volume of enclosure is proportional to the air gap, whereas the coupling coefficients are constant (see Eq. (17)). This implies that the mass normalized acoustic–disk couplings are inversely proportional to the air gap. Consequently, the larger the mass normalized $\mathbf{L}_{nm}^{a,b}$, the less abrupt is the veering between disk-dominated and acoustic-dominated eigenvalues. For example, the acoustic–structure coupling in Fig. 9(a) is stronger than that in Fig. 8(a). At zero rotation speed, the (3,0) mode frequency of the asymmetrically positioned disk in a small air gap is about 3% smaller than that of the symmetrically positioned disk in a large air gap.
(2) An asymmetrically placed disk coupled with acoustic oscillations shows essentially the same instability mechanisms in the absence of dissipation as the symmetric case, i.e., mode coalescence leads to flutter instability.
(3) The onset of instability and its range are also changed somewhat due to the different amount of coupling. As an example, the flutter instability occurs at lower rotating speed when the air gap is smaller.
(4) For the case of long cylindrical enclosures (large air gaps), the higher z-directional acoustic modes such as the (3,0,1) mode also couple to disk vibrations. Consequently, additional instabilities due to coalescence of disk and the higher z-directional acoustic modes also occur at higher speed ranges.

5. Effect of rotating bulk fluid flow

The effect of the rotating bulk fluid flow on the acoustic–structure interactions and instability mechanisms is now investigated. The disk is placed symmetrically in the enclosure with 1 cm air gaps and a 2 mm radial clearance, and the system parameters are listed in Table 1. The coupled discretized equations (25) were initially derived in the *fluid-fixed rotating system*. However, the final results can be easily converted to the *ground-fixed frame* using a coordinate transformation.

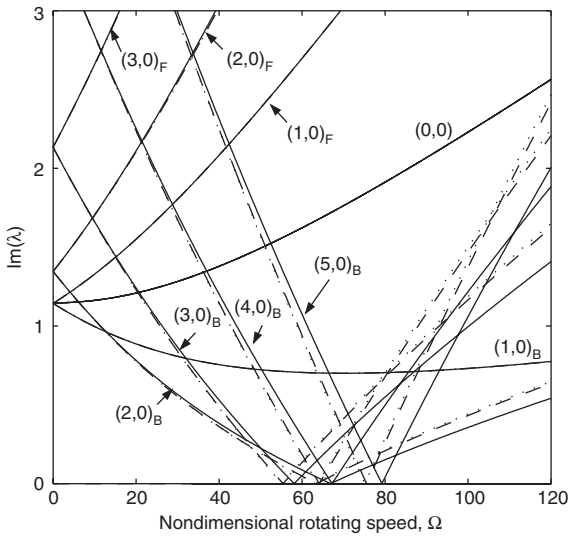

Fig. 10. Nondimensionalized natural frequencies of coupled disk modes in the absence and presence of rotating base flow in an enclosure: - - -, without rotating flow; - · -, with 10% rotating flow; —, with 30% rotating flow. No disk or enclosure damping is included, but 2 mm radial clearance is used in this computation.

Nondimensionalized coupled natural frequencies of the disk-dominated modes are plotted as a function of disk rotation speed in Fig. 10, both in the absence and presence of the rotating base flow. In this example, the circumferential speed of the rotating base flow is assumed as 10% or 30% of the disk rotating speed. In the

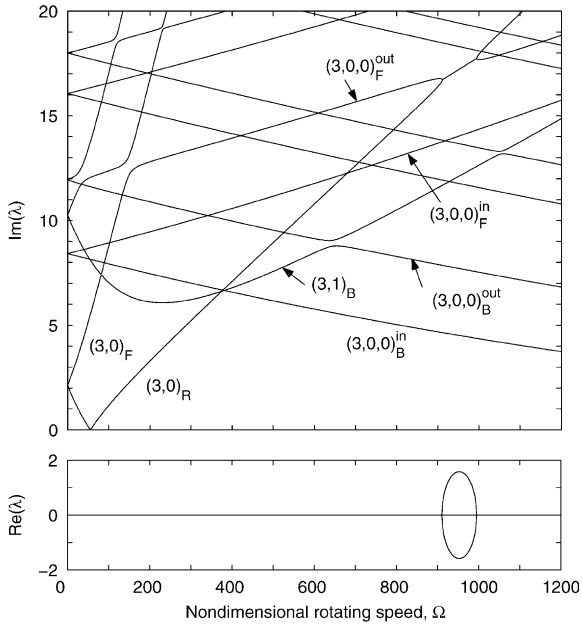

Fig. 11. Real and imaginary part of nondimensionalized three nodal diameter coupled eigenvalues of the disk in the presence of rotating fluid flow ($\Omega_f = 0.1 * \Omega_d$). No disk or acoustic damping is included, but 2 mm radial clearance is present in this computation.

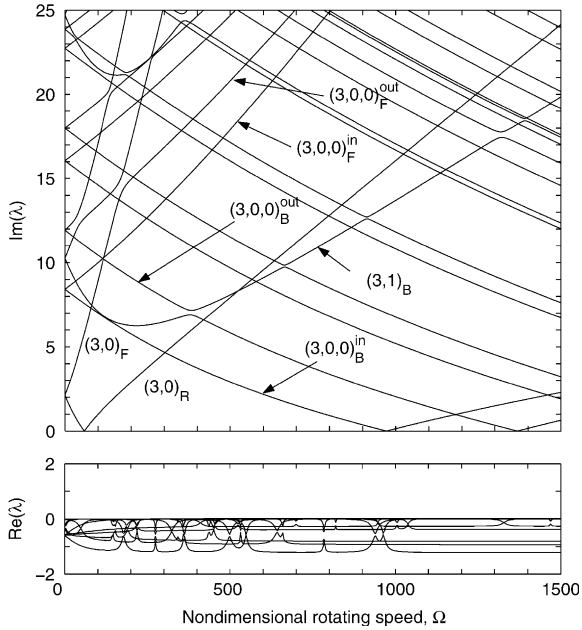

Fig. 12. Real and imaginary part of nondimensionalized three nodal diameter coupled eigenvalues of the disk in the presence of rotating fluid flow ($\Omega_f = 0.3 * \Omega_d$). No disk or acoustic damping is included, but 2 mm radial clearance is present in this computation.

accompanying paper on experimental analysis of this problem, it is estimated that $\Omega_f \sim 30\%\ \Omega_d$. Interestingly at subcritical speed, the coupled frequencies of the disk in the presence of rotating base flow are slightly greater than those in its absence. Consequently, critical speeds of the disk in the presence of 30% rotating flow are about 5% higher than those in its absence. However, at supercritical speed, the coupled frequencies in the presence of rotating flow are slightly decreased.

More interesting features appear in the acoustic-dominated modes at supercritical speed ranges, as shown in Fig. 11. Only the three nodal diameter coupled acoustic–structural modes both in the absence and presence of a rotating base flow are described in the figure. First, as the surrounding fluid rotates at 10% of disk rotation speed, both the in-phase and out-of-phase acoustic modes split into FTW and BTW. It is important to note that in the absence of fluid rotation the frequencies of the in-phase acoustic modes do not split into FTW and BTW. Secondly, flutter instability through mode coalescence occurs at a much higher speed (about 45% higher) than in the absence of rotating fluid flow. On the other hand, when the bulk fluid flow rotates with 30% of disk rotation, no mode coalescence occurs (see Fig. 12). Because the frequencies of the (3,0,0) out-of-phase FTW mode increase faster than that of the (3,0) RTW mode, they do not coalesce in the given speed range and consequently the system remains stable. However as will be shown later, in the presence of fluid viscous damping, the system destabilizes before the rotating speed of mode coalescence.

In summary, the presence of rotating fluid flow changes the disk critical speed, increases the flutter speed for mode coalescence, and splits all acoustic-dominated modes into FTWs and BTWs. It is also reasonable to expect that similar results will hold for the case of an asymmetrically positioned disk–acoustic system.

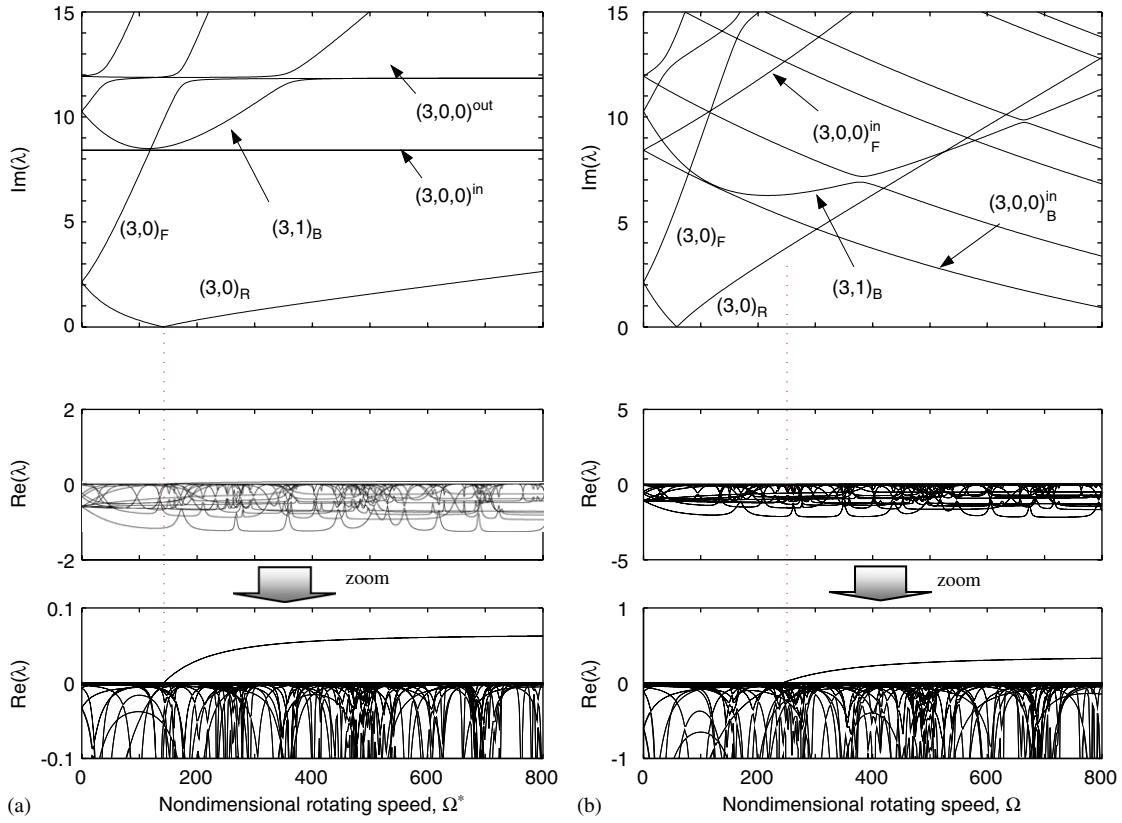

Fig. 13. Real and imaginary parts of nondimensionalized three nodal diameter coupled eigenvalues: (a) in fluid-fixed rotating frame, (b) in ground-fixed frame. Fluid viscous damping is included with 30% of the disk rotating speed.

6. Effect of dissipation

The analysis so far has focused on the instability mechanisms and acoustic–structure interactions in the absence of dissipation. However, in reality there are several kinds of dissipations in the system that need be considered, for instance disk internal damping, acoustic damping, and fluid viscosity.

Let us first consider the effects of viscous fluid damping. Because the potential core of the fluid rotates rigidly at an angular velocity Ω_f, it is reasonable to assume that the fluid viscous damping can be modeled as a positive definite damping in the fluid-fixed reference frame. Therefore, in the presence of fluid viscous damping alone, the system is a gyroscopic system with positive definite damping in the fluid-fixed rotating coordinate system. From this we can immediately conclude that the disk will destabilize at its critical speed (relative to the fluid-fixed frame) due to the classical dissipation-induced destabilization of gyroscopic systems (Kelvin-Tait and Chetaev theorem [43]). Further, this instability involves only one system mode and is different from the mode coalescence induced flutter encountered in the absence of dissipation.

As an example, the coupled eigenvalues in the presence of fluid viscosity damping alone are calculated in the fluid-fixed rotating frame (see Fig. 13(a)). In this computation, the rotating speed of the fluid viscous damping is assumed to be 30% of the disk rotation speed. This calculation is performed after including a positive definite damping in the fluid-fixed reference frame in Eq. (9). As predicted, flutter occurs at the critical speed in this coordinate system. However, in the ground-fixed frame this is a flutter instability occurring at supercritical speed (see Fig. 13(b)). However, this flutter speed is much lower than the rotating speed corresponding to mode coalescence.

The effects of acoustic- and disk-induced damping were considered in a previous work by the authors [16]. It was shown that in the presence of acoustic damping alone, dissipation could be modeled as a positive definite damping in the ground-fixed frame in the discretized equations. Following the KTC theorem therefore, a traveling wave mode destabilizes exactly at its critical speed in the ground-fixed frame. It was also shown by the authors in Ref. [16] that in the presence of disk material damping alone, a different single traveling wave mode instability arises. This instability can also be explained using the KTC theorem, albeit in the disk-fixed rotating frame. The unstable wave is an acoustic-dominated FTW and then instability also occurs at speeds below the speed for mode coalescence.

It is clear that in the presence of combined fluid viscous, acoustic or disk material damping, the system destabilizes via a single traveling wave instability. Whether the unstable wave is a reflected disk-dominated wave or forward traveling acoustic-dominated wave depends on the proportion of disk material damping in the overall damping. Further, these dissipation-induced instabilities will inevitably occur at speeds below the speed at which mode coalescence occurs. Clearly, in spite of the effects of disk–acoustic coupling, the underlying instability mechanisms observed in experiments are likely to be dissipation-induced single mode traveling wave flutter phenomena. However disk–acoustic coupling significantly affects the coupled system eigenvalues prior to flutter instability.

7. Conclusions

The effects of geometric perturbations and the rotating bulk fluid flows on the acoustic–structure interactions and dynamic stability of a flexible disk rotating in an enclosed compressible fluid are investigated theoretically. The main conclusions of the paper are:

(1) The presence of radial clearance modifies significantly the acoustic–structure coupling in the problem. In the absence of any dissipation, the radial clearance does not affect the mechanism of instability, i.e., mode coalescence leads to flutter at supercritical speeds. However, the presence of radial clearance leads to higher speeds of mode coalescence induced flutter.
(2) Asymmetric positioning of the disk significantly modifies the acoustic–structure coupling. It however has no significant effect on the mode coalescence instability mechanism. However, the flutter speed and range are modified somewhat due to the different amount of coupling between the disk and upper and lower enclosures.

(3) The presence of bulk rotating fluid flow increases the flutter speed for mode coalescence, and splits all acoustic-dominated modes into forward and BTWs. This effect is quite significant and at sufficiently high bulk fluid rotation speeds, the mode coalescence instability can vanish for certain system modes.
(4) The presence of fluid viscous, acoustic and disk dampings have a profound effect on the system stability. While the acoustic–structure interactions are not affected, dissipation can cause a single mode traveling wave flutter to occur. Depending on the different contributions to overall damping, this instability occurs somewhere between the disk critical speed in the ground-fixed frame and the mode coalescence speed. Moreover, the unstable wave can take the form of an acoustic-dominated FTW or a disk-dominated reflected traveling wave. It is anticipated that this dissipation-induced instability mechanism is more likely to be observed in experiments than the mode coalescence induced instability.

Acknowledgements

The authors thank the Purdue Research Foundation, Seagate Technology, and the National Science Foundation (NSF) for financial support provided under Award (CAREER) 0134455-CMS. The authors would also like to thank Professors J.S. Bolton and A.K. Bajaj (Purdue University) and S. Tadepalli (Seagate Technology) for fruitful discussion during the course of this research.

Appendix A. Components of the generalized coordinated and submatrices defined in Eq. (21)

$$
\begin{aligned}
a_n &= [a_{000}, \ldots, a_{0n_2n_3}, a^C_{100}, \ldots, a^C_{n_1n_2n_3}, a^S_{100}, \ldots, a^S_{n_1n_2n_3}]^{\mathrm{T}},\\
b_n &= [b_{000}, \ldots, b_{0n_2n_3}, b^C_{100}, \ldots, b^C_{n_1n_2n_3}, b^S_{100}, \ldots, b^S_{n_1n_2n_3}]^{\mathrm{T}},\\
q_m &= [q_{00}, \ldots, q_{0m_2}, q^C_{10}, \ldots, q^C_{m_1m_2}, q^S_{10}, \ldots, q^S_{m_1m_2}]^{\mathrm{T}},\\
u_r &= [u_{00}, \ldots, u_{0r_2}, u^C_{10}, \ldots, u^C_{r_1r_2}, u^S_{10}, \ldots, u^S_{r_1r_2}]^{\mathrm{T}},
\end{aligned}
$$

$$
\mathbf{M}_{a,b} = \frac{\Lambda V^{a,b}}{C^2}\begin{bmatrix}\mathbf{M}_n & & \\ & \mathbf{M}^C_n & \\ & & \mathbf{M}^S_n\end{bmatrix}^{a,b}, \quad \mathbf{M}_q = \begin{bmatrix}\mathbf{1} & & \\ & \mathbf{1} & \\ & & \mathbf{1}\end{bmatrix},
$$

$$
\mathbf{L}_{aq,bq} = \Lambda A_d\begin{bmatrix}\mathbf{L}_{nm} & & \\ & \mathbf{L}^C_{nm} & \\ & & \mathbf{L}^S_{nm}\end{bmatrix}^{a,b}, \quad \mathbf{N}_{au,bu} = \Lambda A_u\begin{bmatrix}\mathbf{N}_{nr} & & \\ & \mathbf{N}^C_{nr} & \\ & & \mathbf{N}^S_{nr}\end{bmatrix}^{a,b},
$$

$$
\mathbf{G}_q = 2\Omega^*\begin{bmatrix}\mathbf{0} & & \\ & & m_1 \\ & -m_1^{\mathrm{T}} & \end{bmatrix},
$$

$$
\mathbf{K}_{a,b} = \frac{\Lambda V^{a,b}}{C^2}\begin{bmatrix}\mathbf{M}_n\boldsymbol{\Lambda}^2_n & & \\ & \mathbf{M}^C_n\boldsymbol{\Lambda}^2_n & \\ & & \mathbf{M}^S_n\boldsymbol{\Lambda}^2_n\end{bmatrix}^{a,b}, \quad \mathbf{K}_q = \begin{bmatrix}k_m & & \\ & k_m & \\ & & k_m\end{bmatrix},
$$

where all submatrices are diagonal except $\mathbf{L}_{nm}$ and $\mathbf{N}_{nr}$, and each element is defined by the corresponding scalar variable in the text.

Appendix B. Derivation of the reduced discretized coupled equation (26)

Consider the singular GNHEP in Eq. (23),

$$\left[\begin{array}{c|ccc} \mathbf{K}_{nn}-\omega^2\mathbf{M}_{nn} & & & \\ \hline & \mathbf{K}_{nn}-\omega^2\mathbf{M}_{nn} & -2\omega\mathbf{L}_{nm} & -2\omega\mathbf{N}_{nr} \\ & \omega\mathbf{L}_{nm}^T & \mathbf{K}_q+\omega\mathbf{G}_q-\omega^2\mathbf{M}_q & \\ & \omega\mathbf{N}_{nr}^T & & \mathbf{0} \end{array}\right]\left\{\begin{array}{c} a_n+b_n \\ b_n-a_n \\ q_m \\ u_r \end{array}\right\}=0. \tag{23'}$$

To overcome the singularities in the last row equation, we define transformation matrix, $\mathbf{T}$, such as

$$b_n^*=\left\{\begin{array}{c} b_c^* \\ b_u^* \end{array}\right\}_n \quad \text{and} \quad \mathbf{N}_{nr}=\left[\begin{array}{c} \mathbf{N}_c \\ \mathbf{N}_u \end{array}\right]_{nr}. \tag{24'}$$

Then, consequently, we obtain from the constraint equations (last row equations in Eq. (23′))

$$\mathbf{N}_{nr}^{\mathrm{T}}\mathbf{T}\dot{b}_u^*=0. \tag{B.1}$$

Now, utilizing Eq. (24′), rewrite the coupled acoustic equations in Eq. (23′) in terms of unconstraint generalized coordinates,

$$\mathbf{M}_{nn}\mathbf{T}\ddot{b}_u^*-2\mathbf{L}_{nm}\dot{q}_m^*-2\mathbf{N}_{nr}\dot{u}_r^*+\mathbf{K}_{nn}\mathbf{T}b_u^*=\mathbf{0}, \tag{B.2}$$

and premultiply Eq. (B.2) by $\mathbf{T}^{\mathrm{T}}$ to obtain

$$\mathbf{T}^{\mathrm{T}}\mathbf{M}_{nn}\mathbf{T}\ddot{b}_u^*-2\mathbf{T}^{\mathrm{T}}\mathbf{L}_{nm}\dot{q}_m^*-2\mathbf{T}^{\mathrm{T}}\mathbf{N}_{nr}\dot{u}_r^*+\mathbf{T}^{\mathrm{T}}\mathbf{K}_{nn}\mathbf{T}b_u^*=\mathbf{0}. \tag{B.3}$$

Since we know that $\mathbf{N}_{nr}^{\mathrm{T}}\mathbf{T}=0$ or $\mathbf{T}^{\mathrm{T}}\mathbf{N}_{\mathrm{nr}}=0$ from Eqs. (B.1) and (B.3) is simplified as

$$\mathbf{T}^{\mathrm{T}}\mathbf{M}_{nn}\mathbf{T}\ddot{b}_u^*-2\mathbf{T}^{\mathrm{T}}\mathbf{L}_{nm}\dot{q}_m^*+\mathbf{T}^{\mathrm{T}}\mathbf{K}_{nn}\mathbf{T}b_u^*=\mathbf{0}. \tag{B.4}$$

Similarly, applying Eq. (24′) to the coupled disk equation in Eq. (23′) yields

$$\mathbf{M}_q\ddot{q}_m^*+\mathbf{L}_{nm}^{\mathrm{T}}\mathbf{T}\dot{b}_u^*+\mathbf{G}_q\dot{q}_m^*+\mathbf{K}_qq_m^*=\mathbf{0} \tag{B.5}$$

and therefore we obtain

$$\left[\begin{array}{cc} \mathbf{T}^{\mathrm{T}}\mathbf{M}_{nn}\mathbf{T} & \\ & 2\mathbf{M}_q \end{array}\right]\left\{\begin{array}{c} \ddot{b}_u^* \\ \ddot{q}_m^* \end{array}\right\}+2\left[\begin{array}{cc} & -\mathbf{T}^{\mathrm{T}}\mathbf{L}_{nm} \\ (\mathbf{T}^{\mathrm{T}}\mathbf{L}_{nm})^{\mathrm{T}} & \mathbf{G}_q \end{array}\right]\left\{\begin{array}{c} \dot{b}_u^* \\ \dot{q}_m^* \end{array}\right\}+\left[\begin{array}{cc} \mathbf{T}^{\mathrm{T}}\mathbf{K}_{nn}\mathbf{T} & \\ & 2\mathbf{K}_q \end{array}\right]\left\{\begin{array}{c} b_u^* \\ q_m^* \end{array}\right\}=0. \tag{26'}$$

References

[1] C. D'Angelo, C.D. Mote Jr., Aerodynamically excited vibration and flutter of a thin disk rotating at supercritical speed, *Journal of Sound and Vibration* 168 (1) (1993) 15–30.

[2] C. D'Angelo, C.D. Mote Jr., Natural frequencies of a thin disk clamped by thick collars with friction at the contacting surfaces spinning at high rotating speed, *Journal of Sound and Vibration* 168 (1) (1993) 1–14.

[3] K.S. Chen, S.M. Spearing, N.M. Nemeth, Structural design of a silicon micro-turbo-generator, *AIAA Journal* 39 (4) (2001) 720–728.

[4] C.A. Serra, M.R. Wiesner, J.M. Laine, Rotating membrane disk filters: design evaluation using computational fluid dynamics, *Chemical Engineering Journal* 72 (1999) 1–17.

[5] F.Y. Huang, C.D. Mote Jr., On the instability mechanisms of a disk rotating close to a rigid surface, *ASME Journal of Applied Mechanics* 62 (1995) 764–771.

[6] F.Y. Huang, C.D. Mote Jr., Mathematical analysis of stability of a spinning disk under rotating arbitrarily large damping forces, *ASME Journal of Applied Mechanics* 118 (1996) 657–662.

[7] G. Naganathan, S. Ramadhayani, A.K. Bajaj, Numerical simulations of flutter instability of a flexible disk rotating close to a rigid wall, *Journal of Vibration and Control* 9 (1) (2003) 95–118.

[8] A.A. Renshaw, Critical speed for floppy disks, *ASME Journal of Applied Mechanics* 65 (1998) 116–120.

[9] H. Hosaka, S.H. Crandall, Self-excited vibrations of a flexible disk rotating on an air film above a flat surface, *Acta Mechanica* 3 (1992) 115–127.

[10] M. Hansen, A. Raman, C.D. Mote Jr., Estimation of nonconservative aerodynamic pressure leading to flutter of spinning disks, *Journal of Fluids and Structures* 15 (2001) 39–57.
[11] B.C. Kim, A. Raman, C.D. Mote Jr., Prediction of aeroelastic flutter in a hard disk drive, *Journal of Sound and Vibration* 238 (2) (2000) 309–325.
[12] M. Hansen, Aeroelasticity and dynamics of spinning disks, Ph.D. Thesis, Technical University of Denmark, 1999.
[13] J.S. Park, I.Y. Shen, Aerodynamically and structurally coupled vibration of multiple co-rotating disks, *ASME Journal of Vibration and Acoustics* 126 (2004) 220–228.
[14] C.O. Orgun, B.H. Tongue, On localization in coupled, spinning, circular plates, *ASME Journal of Vibration and Acoustics* 116 (1994) 555–561.
[15] A.A. Renshaw, C. D'Angelo, C.D. Mote Jr., Aeroelastically excited vibration of a rotating disk, *Journal of Sound and Vibration* 177 (5) (1994) 577–590.
[16] N. Kang, A. Raman, Aeroelastic flutter mechanisms of a flexible disk rotating in an enclosed compressible fluid, *ASME Journal of Applied Mechanics* 71 (2004) 120–130.
[17] A.E. Love, *Treatise on the Mathematical Theory of Elasticity*, Dover Publications, New York, 1944.
[18] T. Von Kármán, Über laminare und turbulente reibung, *Zeitschrift für Angewandte Mathematik und Mechanik* 1 (1921) 233–252.
[19] G.K. Batchelor, Note on a class of solutions of the Navier–Stokes equations representing steady rotationally symmetric flow, *Quarterly Journal of Mechanics and Applied Mathematics* 4 (1951) 29–41.
[20] K. Stewartson, On the flow between two rotating coaxial disks, *Proceedings of the Cambridge Philosophical Society, Mathematical and Physical Sciences* 49 (1953) 333–341.
[21] J.F. Brady, L. Durlofsky, On rotating disk flow, *Journal of Fluid Mechanics* 175 (1987) 363–394.
[22] A.Z. Szeri, S.J. Schneider, F. Labbe, H.N. Kaufman, Flow between rotating disks. Part 1. Basic flow, *Journal of Fluid Mechanics* 134 (1983) 103–131.
[23] C.A. Schuler, W. Usry, B. Weber, J.A.C. Humphrey, R. Greif, On the flow in the unobstructed space between shrouded corotating disks, *Physics of Fluids A* 2 (10) (1990) 1760–1770.
[24] D. Dijkstra, G.J.F. Van Heijist, The flow between two finite rotating disks enclosed by a cylinder, *Journal of Fluid Mechanics* 128 (1983) 123–154.
[25] M.P. Escudier, Observations of the flow produced in a cylindrical container by a rotating endwall, *Experiments in Fluids* 2 (1984) 189–196.
[26] C.Y. Soong, C.C. Wu, T.P. Liu, Flow structure between two co-axial disks rotating independently, *Experimental Thermal and Fluid Science* 27 (2003) 295–311.
[27] M. Watanabe, F. Hara, Theoretical instability analysis of a rotating flexible disk subjected to swirling fluid flow, *Fluid–Structure Interaction, Aeroelasticity, Fluid-Induced Vibration and Noise* 2 (AD53-2) (1997) 57–66.
[28] S. Imai, Fluid dynamics mechanism of disk flutter by measuring the pressure between disks, *IEEE Transactions on Magnetics* 37 (2) (2001) 837–841.
[29] M. Al-Shannag, J. Herrero, J.A.C. Humphrey, F. Giralt, Effect of radial clearance on the flow between corotating disks in fixed cylindrical enclosures, *Journal of Fluids Engineering* 124 (2002) 719–727.
[30] M. Tatewaki, N. Tsuda, T. Maruyama, An analysis of disk flutter in hard disk drives in aerodynamic simulations, *IEEE Transactions on Magnetics* 37 (2) (2001) 842–846.
[31] H. Shimizu, M. Tokuyama, S. Imai, S. Nakamura, K. Sakai, Study of aerodynamic characteristics in hard disk drives by numerical simulation, *IEEE Transactions on Magnetics* 37 (2) (2001) 831–836.
[32] E.H. Dowell, *Aeroelasticity of Plates and Shells*, Noordhoff International Publishing, Leyden, 1975.
[33] D.T. Blackstock, *Fundamentals of Physical Acoustics*, Wiley, New York, 2000.
[34] E.H. Dowell, G.F. Gorman, D.A. Smith, Acoustoelasticity: general theory, acoustic natural modes and forced response to sinusoidal excitation, including comparisons with experiment, *Journal of Sound and Vibration* 52 (4) (1977) 519–542.
[35] F. Fahy, *Sound and Structural Vibration*, Academic Press, London, 1985.
[36] P.M. Morse, K.U. Ingard, *Theoretical Acoustics*, Princeton University Press, New Jersey, 1968.
[37] D.T. Greenwood, *Classical Dynamics*, Dover Publications, New York, 1997.
[38] V.B. Bokil, U.S. Shirahatti, A technique for the modal analysis of sound-structure interaction problems, *Journal of Sound and Vibration* 173 (1) (1994) 23–41.
[39] Z. Bai, J.W. Demmel, J. Dongarra, A. Ruhe, H. van der Vorst, *Templates for the Solution of Algebraic Eigenvalue Problems: A Practical Guide*, SIAM, Philadelphia, 2000.
[40] J.H. Ginsberg, *Mechanical and Structural Vibrations: Theory and Applications*, Wiley, New York, 2001.
[41] L. Meirovitch, A separation principle for gyroscopic conservative systems, *ASME Journal of Vibration and Acoustics* 119 (1997) 110–119.
[42] R.K. Jha, R.G. Parker, Spatial discretization of axially moving media vibration problems, *Journal of Vibration and Acoustics* 122 (2000) 290–294.
[43] D.R. Merkin, *Introduction to the Theory of Stability*, Springer, New York, 1997.